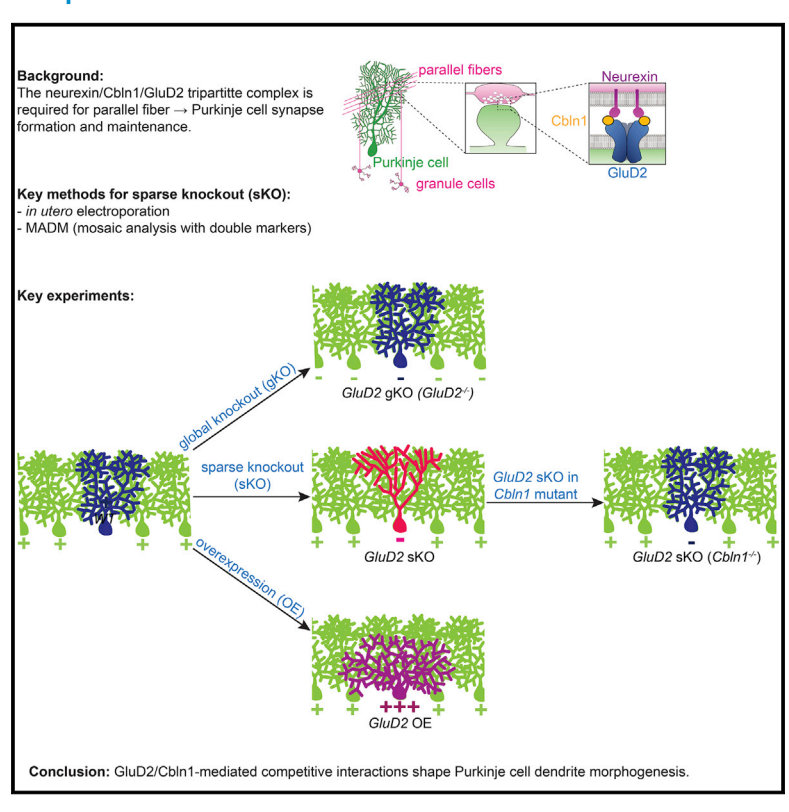
# **Neuron**

# GluD2- and Cbln1-mediated competitive interactions shape the dendritic arbors of cerebellar Purkinje cells

# **Graphical Abstract**



# **Authors**

Yukari H. Takeo, S. Andrew Shuster, Linnie Jiang, ..., Mark J. Wagner, Surya Ganguli, Liqun Luo

# Correspondence

lluo@stanford.edu

# In Brief

Takeo and Shuster et al. find that sparse but not global disruption of GluD2, a synapse organizer, alters cerebellar Purkinje cell dendrite morphology. Genetic experiments and theoretical modeling suggest that a Purkinje cell's ability to compete for forming synapses with its presynaptic partners in turn regulates its dendrite branching.

# **Highlights**

- Sparse but not global GluD2 knockout disrupts Purkinje cell dendrite morphogenesis
- GluD2 sparse knockout reduces initial but increases subsequent dendritic branching
- Competitive dendrite morphogenesis requires GluD2 interactions with ligand Cbln1
- A generative model of dendrite growth recapitulates GluD2 manipulation phenotypes





# **Neuron**



# **Article**

# GluD2- and Cbln1-mediated competitive interactions shape the dendritic arbors of cerebellar Purkinje cells

Yukari H. Takeo, <sup>1,6</sup> S. Andrew Shuster, <sup>1,2,6</sup> Linnie Jiang, <sup>2</sup> Miley C. Hu, <sup>1</sup> David J. Luginbuhl, <sup>1</sup> Thomas Rülicke, <sup>3</sup> Ximena Contreras, <sup>4</sup> Simon Hippenmeyer, <sup>4</sup> Mark J. Wagner, <sup>1</sup> Surya Ganguli, <sup>5</sup> and Liqun Luo<sup>1,7,\*</sup>

<sup>1</sup>Department of Biology, Howard Hughes Medical Institute, Stanford University, Stanford, CA 94305, USA

\*Correspondence: Iluo@stanford.edu https://doi.org/10.1016/j.neuron.2020.11.028

#### SUMMARY

The synaptotrophic hypothesis posits that synapse formation stabilizes dendritic branches, but this hypothesis has not been causally tested *in vivo* in the mammalian brain. The presynaptic ligand cerebellin-1 (Cbln1) and postsynaptic receptor GluD2 mediate synaptogenesis between granule cells and Purkinje cells in the molecular layer of the cerebellar cortex. Here we show that sparse but not global knockout of *GluD2* causes under-elaboration of Purkinje cell dendrites in the deep molecular layer and overelaboration in the superficial molecular layer. Developmental, overexpression, structure-function, and genetic epistasis analyses indicate that these dendrite morphogenesis defects result from a deficit in Cbln1/GluD2-dependent competitive interactions. A generative model of dendrite growth based on competitive synaptogenesis largely recapitulates *GluD2* sparse and global knockout phenotypes. Our results support the synaptotrophic hypothesis at initial stages of dendrite development, suggest a second mode in which cumulative synapse formation inhibits further dendrite growth, and highlight the importance of competition in dendrite morphogenesis.

#### **INTRODUCTION**

Nervous system function requires proper dendrite morphogenesis and synapse formation. Disruptions of these processes are associated with many neurodevelopmental and psychiatric disorders, such as autism and schizophrenia (Kulkarni and Firestein, 2012). Research in the past decades has elucidated mechanisms underlying dendrite morphogenesis (Jan and Jan, 2010) and synapse formation (Südhof, 2018; Yogev and Shen, 2014). However, the relationship between these two developmental events is less explored. Dendrite growth is usually considered to occur prior to synapse formation during neuronal differentiation because a neuron must extend dendritic branches before it can form synapses with incoming axons. However, these two processes occur largely concurrently in many cases. Thus, synapse formation and maturation could, in principle, influence dendritic branching and elongation.

Observations of fixed central nervous system tissue led to the synaptotrophic hypothesis of dendrite growth, which postulates that synapse formation and maturation promote dendrite growth

(Cline and Haas, 2008; Vaughn, 1989). Live imaging in amphibians and fish has provided support for this hypothesis: synapse formation and signaling stabilize nascent dendritic branches, allowing them to extend further (Chen et al., 2010; Haas et al., 2006; Niell et al., 2004). Disrupting synaptic activity revealed that it regulates dendrite growth and branching in mammalian spinal motor neurons (Kalb, 1994), but a direct test of the synaptotrophic hypothesis requires *in vivo* manipulation of synapse formation and visualization of dendritic arbors with single-cell resolution. To our knowledge, no such experiments have been performed in the mammalian brain. Here we investigate this relationship by examining the role of glutamate receptor delta 2 (GluD2)—one of the best-characterized synaptogenic proteins—in dendrite morphogenesis.

GluD2 belongs to the ionotropic glutamate receptor family but is atypical in that it neither binds glutamate nor exhibits direct channel activity upon binding of known ligands. However, GluD2 has a well-established role in synapse formation and maintenance; *GluD2* knockout mice lose nearly half of all synapses between the axons of cerebellar granule cells (parallel fibers)



<sup>&</sup>lt;sup>2</sup>Neurosciences Program, Stanford University, Stanford, CA 94305, USA

<sup>&</sup>lt;sup>3</sup>Institute of Laboratory Animal Science, University of Veterinary Medicine Vienna, Vienna, Austria

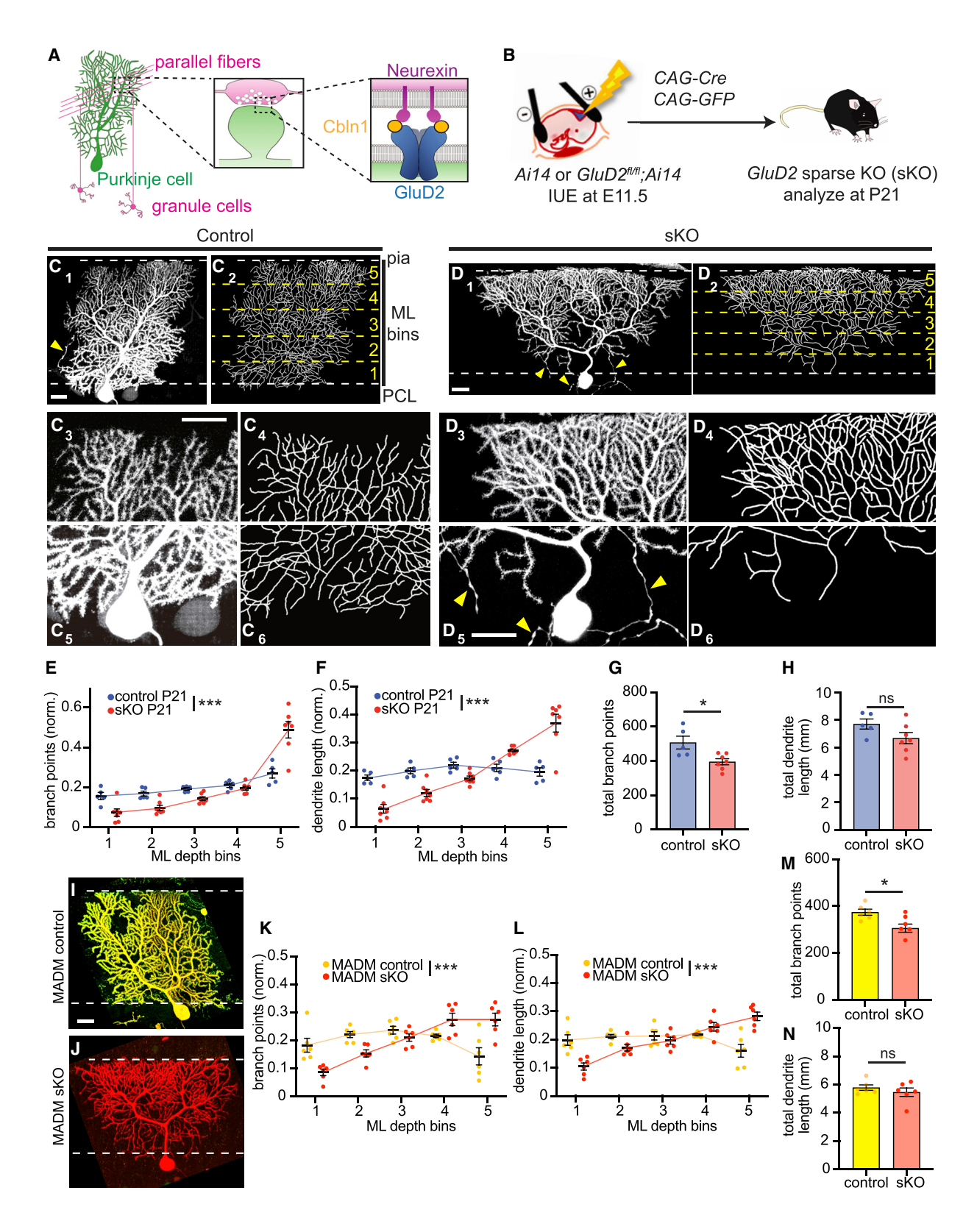
<sup>&</sup>lt;sup>4</sup>Institute of Science and Technology Austria, Am Campus 1, 3400 Klosterneuburg, Austria

<sup>&</sup>lt;sup>5</sup>Department of Applied Physics, Stanford University, Stanford, CA 94305, USA

<sup>&</sup>lt;sup>6</sup>These authors contributed equally

<sup>&</sup>lt;sup>7</sup>Lead contact







and the dendrites of Purkinje cells at the ultrastructural level (Ichikawa et al., 2016; Kashiwabuchi et al., 1995), concomitant with a reduction in physiological responses of Purkinje cells to parallel fiber activation (Kurihara et al., 1997). GluD2 on Purkinje cell dendrites acts as a receptor for cerebellin-1 (Cbln1) secreted by granule cells. Cbln1 also binds neurexin, a presynaptic plasma membrane protein on parallel fibers (Yuzaki, 2017). Thus, neurexin, Cbln1, and GluD2 form a tripartite synaptic adhesion complex that promotes parallel fiber → Purkinje cell synapse formation and maintenance (Matsuda et al., 2010; Uemura et al., 2010; Yuzaki, 2017; Figure 1A). In support of the synaptogenic role of this tripartite complex, Cbln1 knockout also substantially depletes parallel fiber → Purkinje cell synapses, and addition of recombinant Cbln1 in adults rescues this phenotype (Hirai et al., 2005; Matsuda et al., 2010). Indeed, knockout of GluD2 or Cbln1 causes some of the strongest synapse loss defects in mouse knockouts of single genes reported. Thus, GluD2<sup>-/-</sup> Purkinje cells provide an opportunity to examine the effects of disrupting synapse formation and maintenance on dendrite growth.

#### **RESULTS**

# Sparse knockout of GluD2 in Purkinje cells reduces dendritic branching in the deep molecular layer but enhances dendritic branching in the superficial molecular layer

To gain genetic access to developing mouse Purkinje cells, we performed in utero electroporation (IUE) at embryonic day 11.5 (Nishiyama et al., 2012; Takeo et al., 2015). To delete GluD2 in Purkinje cells and examine the morphology of mutant dendrites, we electroporated plasmids expressing Cre recombinase and a fluorescent marker into wild-type (control) or GluD2<sup>fl/fl</sup> embryos (homozygous for a floxed allele of GluD2; Takeuchi et al., 2005; Figure 1B). Typically, only a small fraction of isolated Purkinje cells expressed the plasmids (Nishiyama et al., 2012); thus, the morphology of the entire dendritic arbor could be readily imaged (Figure 1C1) and branching patterns completely traced (Figure 1C2). Likewise, IUE into GluD2fl/fl embryos resulted in GluD2 knockout in a sparse population of Purkinje cells in an otherwise wild-type environment; hereafter we refer to such cells as sparse knockout (sKO) cells. Antibody staining validated that Cre/GFP-expressing cells, but not neighboring cells, lacked GluD2 protein (Figures S1A and S1B).

We first examined the morphology of Purkinje cells at postnatal day 21 (P21), when their dendritic arbors have reached the pial surface. Control dendritic arbors, when viewed face on, typically assumed a nearly rectangular shape in the plane orthogonal to parallel fibers, with similar widths in the deep (close to the Purkinje cell layer) and superficial (close to the pial surface) portions of the molecular layer (Figures 1C and S1C). In contrast, GluD2 sKO Purkinje cells exhibited an inverted triangular shape (Figures 1D and S1D). In the superficial molecular layer, GluD2 sKO cells exhibited much enhanced branching (Figures 1D3 and 1D4) compared with controls (Figures 1C3 and 1C4). Conversely, in the deep molecular layer, GluD2 sKO Purkinje cells exhibited much reduced arbors (Figures 1D5 and 1D6) compared with controls (Figures 1C5 and 1C6). To quantify these effects, we divided the entire molecular layer into five bins of equal depth and quantified the distribution of total dendritic branchpoints and length within each bin following dendrite tracing (Figures 1C and 1D; STAR methods). Compared with controls, GluD2 sKO Purkinje cells had fewer branchpoints and reduced dendritic length in the deepest layer but more branchpoints and increased dendritic length in the most superficial layer (Figures 1E, 1F, S1E, and S1F). When the entire dendritic tree was measured, GluD2 sKO Purkinje cells exhibited fewer total dendritic branchpoints than controls but similar total dendritic length (Figures 1G and 1H).

To validate the GluD2 sKO dendrite morphogenesis phenotypes via an independent method, we used mosaic analysis with

# Figure 1. GluD2 sKO phenotypes in Purkinje cells

(A) Schematic summary. Left: anatomy, morphology, and connectivity of cerebellar granule cells (magenta) and Purkinje cells (green). Center: schematic of parallel fiber → Purkinje cell synapses. Right: the tripartite synaptic adhesion complex.

(B) Schematic of in utero electroporation (IUE) for genetically accessing Purkinje cells in GluD2firl; Ai14 or Ai14 (control) embryos. Plasmids encoding Cre recombinase and GFP were co-injected into the fourth ventricle at embryonic day 11.5 (E11.5). Cerebellar samples were collected at post-natal day 21 (P21).

(C) Control Purkinje cells labeled via IUE exhibit similar levels of dendritic elaboration in the deep and superficial molecular layer at P21. Representative confocal image of a control Purkinje cell (C<sub>1</sub>) and its tracing (C<sub>2</sub>) are magnified for the superficial (C<sub>3</sub> and C<sub>4</sub>) and deep (C<sub>5</sub> and C<sub>6</sub>) molecular layer. The top and bottom dashed lines in (C<sub>1</sub>) and (C<sub>2</sub>) represent boundaries between the molecular layer (ML) and the pial surface (pia) and Purkinje cell layer (PCL), respectively. The yellow dashed lines in (C2) represent divisions between the five numbered ML bins. Yellow arrowheads, Purkinje cell axons.

(D) Same as (C), except that GluD2 is knocked out (sKO) of this isolated Purkinje cell, which exhibits an inverted triangular shape, with overelaboration in the superficial ( $D_3$  and  $D_4$ ) and under-elaboration in the deep ( $D_5$  and  $D_6$ ) ML.

(E and F) Quantification of the number of branchpoints (E) and dendrite length (F) in each ML depth bin in control (blue) and GluD2 sKO (red) Purkinje cells. Data were normalized to the total number of dendritic branchpoints or dendrite length across the tree.

(G and H) Quantification of the total number of branchpoints (G) and length (H) of control and GluD2 sKO Purkinje cells.

(E-H) Data are mean ± SEM; n = 5 control and 7 sKO cells from 2 (control) and 3 (sKO) mice.

(I and J) Representative confocal images of GluD2+/- (I) and GluD2-/- (J) cells produced by MADM.

(K and L) Quantification of the normalized number of branchpoints (K) and dendrite length (L) in each ML depth bin in MADM control (yellow) and GluD2 sKO (red) Purkinje cells.

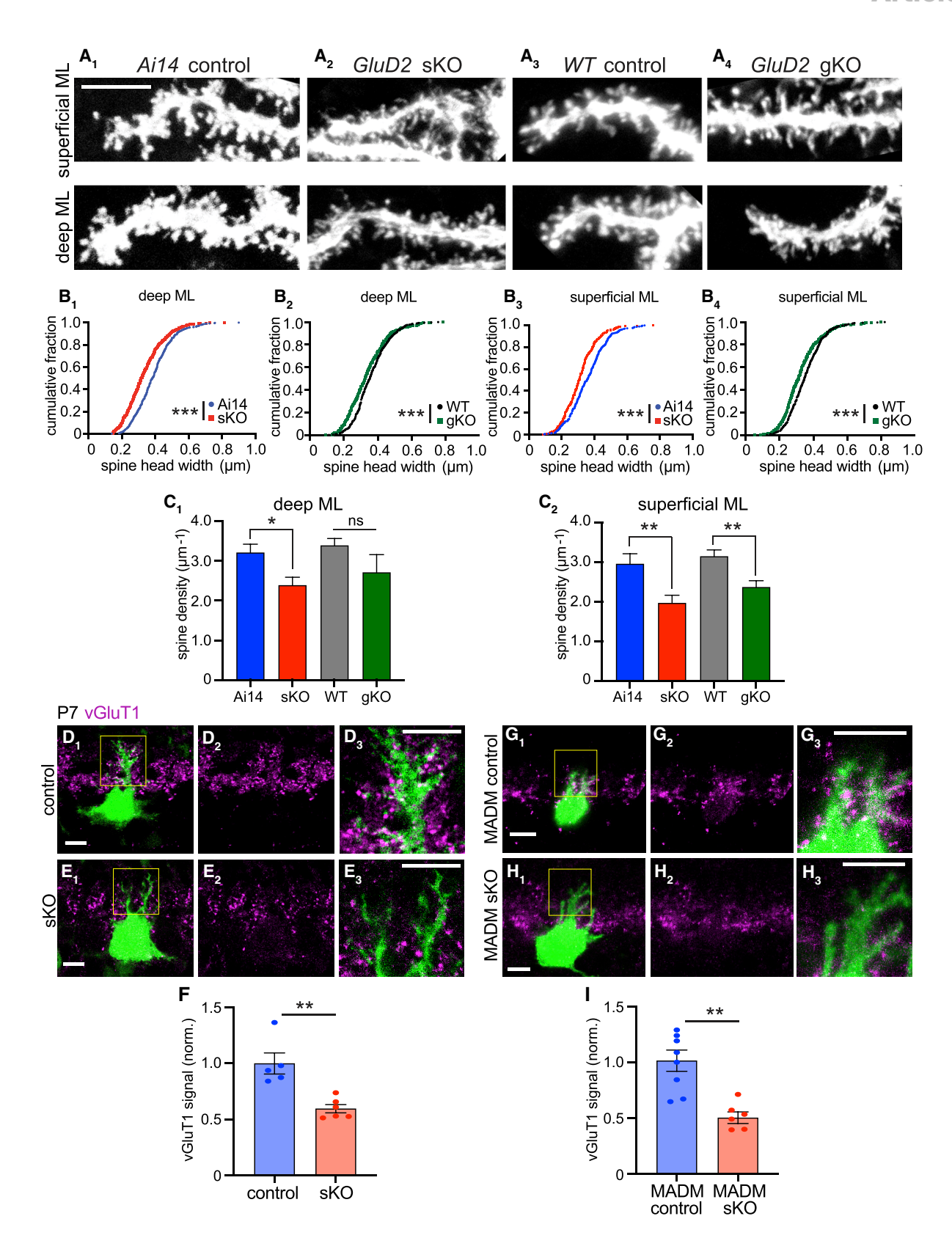
(M and N) Quantification of the total number of branchpoints (M) and dendrite length (N) of MADM control and GluD2 sKO Purkinje cells.

(K-N) Data are mean  $\pm$  SEM; n = 6 GluD2<sup>+/-</sup> control and 6 GluD2<sup>-/-</sup> sKO cells from 2 mice.

Note that the baseline parameters for controls in IUE and MADM experiments (G, H, M, and N) are different (see STAR methods for details), likely caused by a different genetic background. For binned plots in this (E, F, K, and L) and all subsequent figures, p values were calculated using two-way ANOVA between control and experimental values in each bin. For bar plots in this (G, H, M, and N) and all subsequent figures, p values were calculated using unpaired, two-tailed t tests unless otherwise noted. \*p < 0.05, \*\*p < 0.01, \*\*\*p < 0.001. Scale bars, 20  $\mu$ m. See also Figures S1 and S2.









double markers (MADM; Contreras et al., 2020; Zong et al., 2005) to knock out GluD2 in a sparse population of cells uniquely marked in an otherwise GluD2+/- background (Figure S2A). MADM-mediated sKO was also confirmed by loss of GluD2 protein (Figures S2B and S2C). Compared with MADM GluD2+/- controls (Figures 1I and S2D), which resembled wild-type cells, P21 MADM GluD2<sup>-/-</sup> Purkinje cells exhibited dendrite morphogenesis defects similar to those generated via IUE-based sKO, with reduced branching in the deep molecular layer and enhanced branching in the superficial molecular layer (Figures 1J and S2E). Quantifying the distribution of dendritic branches and lengths in five depth bins across the molecular layer revealed phenotypes in MADM GluD2 sKO cells (Figures 1K, 1L, S1G, and S1H), similar to IUE-mediated GluD2 sKO cells (Figures 1E, 1F, S1E, and S1F). MADM GluD2 sKO cells also exhibited fewer total dendritic branch points than controls but similar total dendritic length (Figures 1M and 1N). These findings demonstrate that GluD2, a receptor essential for parallel fiber → Purkinje cell synapse formation, regulates Purkinje cell dendritic branching.

# Evidence that GluD2 sKO phenotypes are related to synaptogenesis defects

Several lines of evidence suggested that GluD2 sKO disrupted synaptogenesis, consistent with the established role of GluD2 in synapse formation and maintenance (Kurihara et al., 1997). First, fine morphological analysis of P21 Purkinje cells revealed that sKO dendrites had fewer mature dendritic spines and more filopodium-like extensions than control dendrites (Figures 2A1 and 2A2). This effect was statistically significant when comparing the head widths of all dendritic protrusions (Figures 2B1 and 2B2) or the density of mature spines (Figures 2C1 and 2C2; see STAR methods for classification criteria). These data suggest that sKO dendrites persist in an immature, exploratory state compared to controls.

Second, previous studies found that climbing fibers (axons from inferior olive neurons), which normally synapse onto Purkinje cell dendrites within the deepest 80% of the molecular layer, invade the superficial-most 20% of the molecular layer when parallel fiber → Purkinje cell synapses are disrupted (Bosman and Konnerth, 2009; Hashimoto et al., 2001; Hirai et al., 2005; Ichikawa et al., 2002). Thus, evidence of climbing fiber superficial over-innervation via vGluT2 staining provides indirect evidence of disrupted parallel fiber → Purkinje cell synapses. GluD2 sKO cells exhibited this phenotype when examined in adults (Figure S3).

Third, we immunostained for vesicular glutamate transporter 1 (vGluT1), a presynaptic marker of parallel fiber → Purkinje cell synapses (Miyazaki et al., 2003), at P7; at this stage, Purkinje cell dendritic branches are not too dense so that most of the vGluT1 signal could be assigned to individual Purkinje cell dendrites in a given plane. In IUE-based (Figures 2D-2F) and MADM (Figures 2G-2I) experiments, we found a significant reduction in vGluT1 intensity abutting GluD2 sKO dendrites compared with controls. This transcellular effect on a presynaptic marker suggests that GluD2 sKO caused a cell-autonomous synaptogenesis defect.

# Global KO of GluD2 does not grossly affect Purkinje cell dendrite morphogenesis

The effects of GluD2 sKO on the shape of Purkinje cell dendritic tree were unexpected, as previous studies of Purkinje cells in germline GluD2 KO animals did not report such phenotypes (Kaneko et al., 2011; Kashiwabuchi et al., 1995). To determine whether the phenotypes are specific to sKO, we sparsely labeled wild-type control and GluD2 germline (global) KO (gKO) Purkinje cells using IUE (Figure 3A). Consistent with previous reports, we did not find gross changes in the morphology of GluD2 gKO Purkinje cell dendritic arbors compared with controls (Figures 3B, 3C, S2F, and S2G; guantified in Figures 3D and 3E). The total number of branchpoints and dendritic length in GluD2 gKO cells were not significantly different from controls (Figures 3F and 3G). Like sKO cells, gKO cells also had fewer mature spines compared with control cells (Figures 2A-2C), consistent with GluD2's essential role in synaptogenesis.

Taken together with the sKO phenotypes, these data reveal that Purkinje cell dendrite morphology is affected more by relative differences in GluD2 signaling between neighboring Purkinje cells than by the absolute level of GluD2 signaling within individual cells. Given the established function of GluD2 in parallel fiber → Purkinje cell synaptogenesis (see also Figures 2 and S3), these data suggest that the GluD2 sKO dendritic branching phenotypes may result from Purkinje cell dendrites competing with their neighbors for synaptogenesis with parallel fibers.

# GluD2 sKO phenotypes arise early and persist into adulthood

When does the GluD2 sKO phenotype arise during development? Cerebellar morphogenesis occurs primarily during the

# Figure 2. Evidence that GluD2 sKO disrupts synaptogenesis

(A) Representative dendritic segments in the deep (bin 1) and superficial (bin 5) ML showing the morphology of dendritic protrusions in P21 Ai14 control (A<sub>1</sub>), GluD2 sKO (A<sub>2</sub>), wild-type (WT) control (A<sub>3</sub>), and GluD2 gKO (A<sub>4</sub>) Purkinje cells at P21. Scale bar, 5  $\mu$ m.

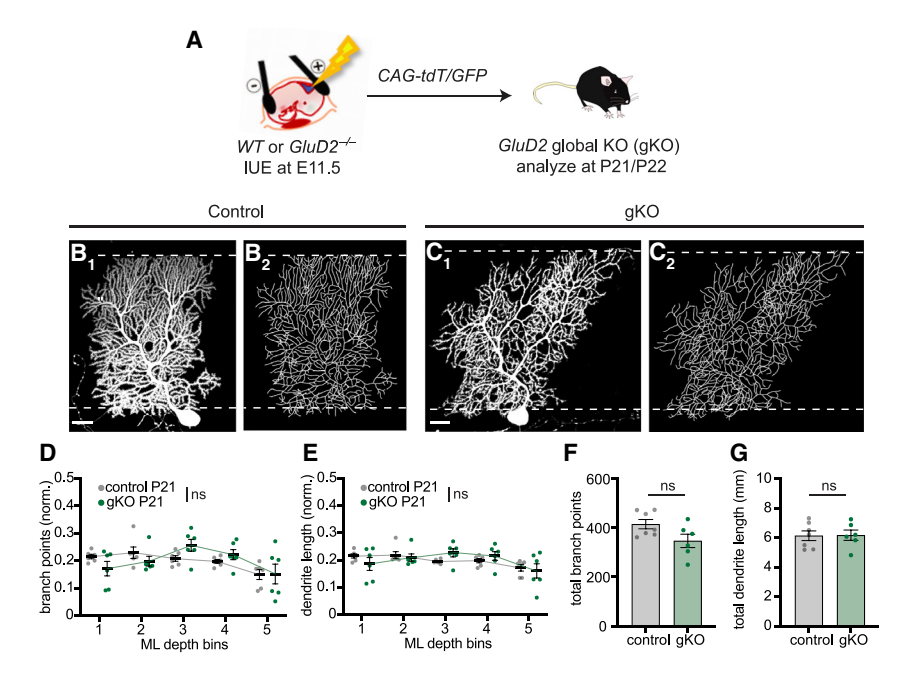
(B) Cumulative distribution of the head widths of dendritic protrusions. n = 444 (Ai14 control), 442 (GluD2 sKO), 405 (WT control), and 414 (GluD2 gKO) deep ML protrusions and n = 417 (Ai14 control), 414 (GluD2 sKO), 383 (WT control), and 453 (GluD2 gKO) superficial ML protrusions. \*\*\*p < 0.001, Kolmogorov-Smirnov test.

(C) Dendritic spine density. Data are mean ± SEM; n = 10 cells for each condition; \*p < 0.05, \*\*p < 0.01; ns, not significant (p > 0.05); t test. (B and C) Data were collected from 2 (Ai14 control), 3 (GluD2 sKO), 2 (WT control), and 2 (GluD2 gKO) mice.

(D, E, G, and H) Representative single-section confocal images of IUE-based (D and E) or MADM-based (G and H) GluD2 sKO Purkinje cells labeled with GFP (D, E, and G) or tdTomato (H) (green). Magenta indicates vGluT1 staining to label presynaptic terminals of parallel fibers. (D2), (D3), (E2), (E3), (G2), (G3), (H2), and (H3) are high-magnification images (vGluT1 only or vGluT1 with GFP or tdTomato) of (D<sub>1</sub>), (E<sub>1</sub>), (G<sub>1</sub>), and (H<sub>1</sub>) (boxed regions). Scale bars, 10 μm.

(F and I) Quantification of normalized vGluT1 intensities on dendrites from IUE (F) and MADM (I) experiments. Data are mean ± SEM; n = 5 (control) and 6 (sKO) cells from 1 control and 1 sKO mice for IUE; n = 8 (control; GluD2+/-) and 6 (MADM sKO; GluD2-/-) cells from 3 mice; \*\*p < 0.01, t test. See also Figure S3.





first three postnatal weeks. At birth, granule cell progenitors occupy the most superficial external granular layer (EGL), where they undergo rapid proliferation. As granule cells exit mitosis, they extend their axons as parallel fibers into the developing molecular layer between EGL and Purkinje cells, whereas their cell bodies descend past the Purkinje cell layer into the internal granular layer, giving rise to the granule cell layer in adults (Altman, 1972a; Figure 4A). Later-born granule cells stack their parallel fibers superficially to those from earlier-born granule cells (Espinosa and Luo, 2008). Developing parallel fibers are the substrate onto which Purkinje cell dendrites grow, branch, and form synapses, expanding the molecular layer in the process. As granule cell neurogenesis proceeds, the EGL is gradually replaced by the molecular layer until P21, when granule cell neurogenesis is complete and Purkinje cell dendrites reach the pial surface (Figure 4A).

To determine how GluD2 regulates dendrite morphogenesis across development, we analyzed the GluD2 sKO phenotype at P7, P10, P14, P21, and ~P63 using IUE (Figure 4B). We found reduced branching in the deep molecular layer and over-branching in the superficial molecular layer of GluD2 sKO cells as early as P10 (Figures 4C1 and 4D1; see P7 analysis in Figures S4A-S4I), after parallel fibers have started to form synapses onto Purkinje cells (Altman, 1972b; West and del Cerro, 1976). These phenotypes persisted across all later stages, with the superficial molecular layer over-branching phenotype becoming more pronounced with age (Figures 4C2-4C4, 4D2-4D4, S4J, and S4K; quantified in Figures 4E and 4F). Notably, at P10, GluD2 sKO cells had more dendritic branches extending beyond the superficial border of the molecular layer than control cells (arrowheads in Figure 4D<sub>1</sub> and Figure S4J<sub>1</sub>; quantified in Figure S4J<sub>2</sub>). Quantification of total dendritic branchpoints, lengths, and average segment lengths (Figure 4G-4I) indicated a general trend of fewer total dendritic branchpoints in sKO cells, reaching statisti-

# Figure 3. GluD2 gKO does not disrupt dendrite morphology

(A) Schematic depicting labeling of Purkinje cells in WT and GluD2<sup>-/-</sup> (gKO) embryos.

(B and C) WT control and GluD2-/- gKO Purkinje cells exhibit similar levels of dendritic elaboration in the deep and superficial ML around P21, as seen in representative confocal images (B1 and C1) and tracings (B2 and  $C_2$ ) of Purkinje cell dendrites. Scale bars, 20  $\mu m$ .

(D and E) Quantification of the normalized number of branchpoints (D) and dendrite length (E) in each

(F and G) Quantification of total number of branchpoints (F) and dendrite length (G) of control (gray) and GluD2 gKO (green) Purkinje cells.

(D-G) Data are mean ± SEM; n = 6 control and 6 gKO cells from 2 control and 2 gKO mice; ns, p > 0.05 by two-way ANOVA (D and E) or t test (F and G).

See also Figures 2 and S2.

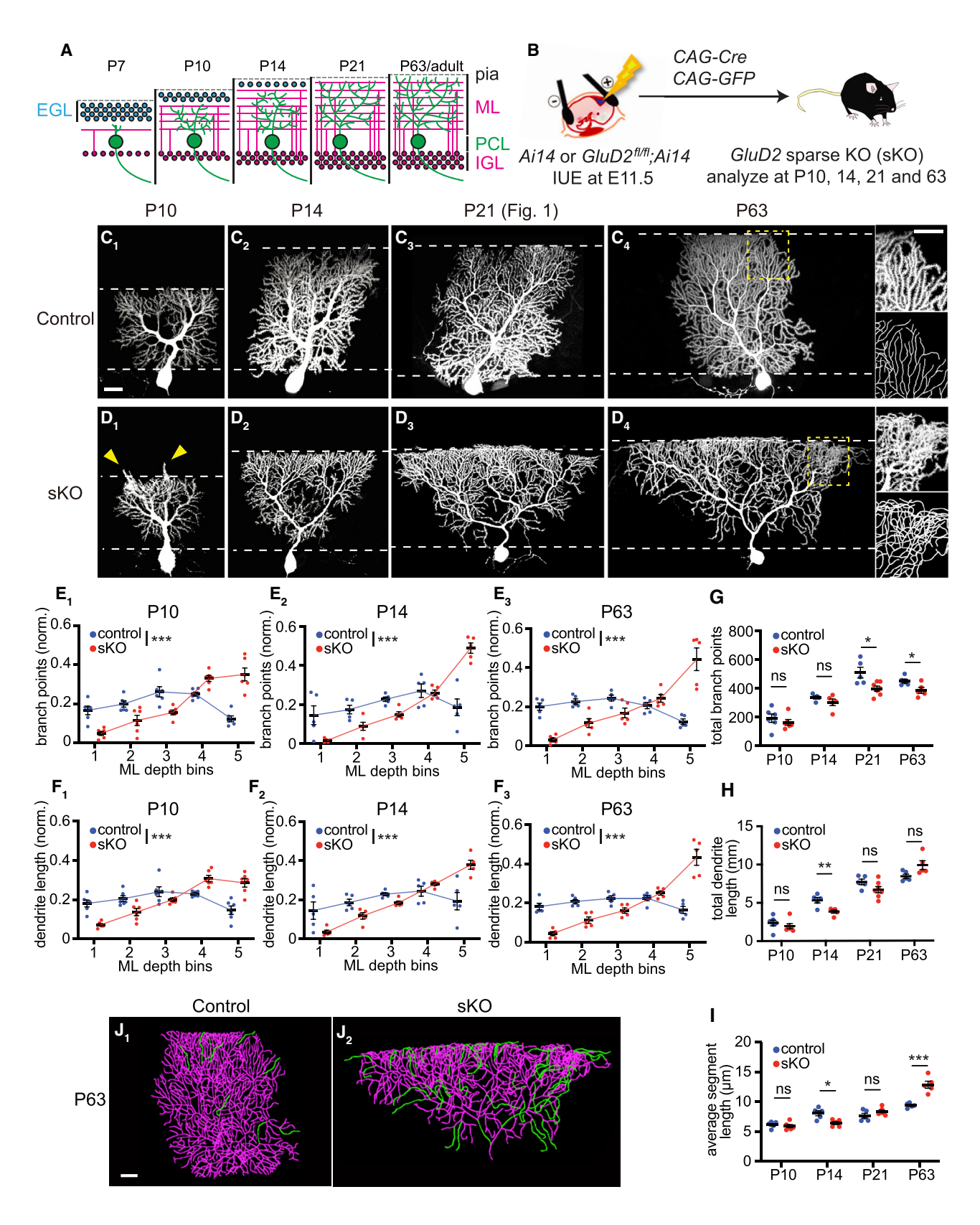
cal significance at P21 and P63 (Figure 4G). A trend of decreased total dendritic length in sKO cells appeared in early stages but was reversed at P63 (Figure 4H). The com-

bination of the above resulted in a highly significant increase in the average dendritic segment length of sKO dendrites compared with controls at P63 (Figure 4I), mostly because of long terminal branches (Figure 4J). In addition, P21 and particularly P63 sKO Purkinje dendritic trees exhibited crossing over of dendritic branches caused by branches that extended out of the 2D plane to which normal dendritic trees are restricted (compare Figures 1D3 and 1D4 with 1C3 and 1C4 and the insets of Figure 4D4 with 4C4). In summary, the GluD2 sKO phenotypes appear early and persist into adulthood.

# GluD2 overexpression causes dendritic over-branching in the deep molecular layer

To complement the sKO studies, we next examined the effects of sparsely overexpressing GluD2 (GluD2 overexpression [OE]) in Purkinje cells of wild-type mice via IUE (Figure 5A). At P7, regions adjacent to GluD2 OE Purkinje cell dendrites exhibited increased vGluT1 staining intensity (Figures 5B and 5C), with vGluT1 staining levels positively correlated with GluD2 OE levels (Figure 5D). These data support a synaptogenic role of GluD2. Compared with controls (Figure 5E), GluD2 OE Purkinje cells also exhibited supernumerary primary dendrites (Figures 5F1 and 5G) and numerous spine-like protrusions from dendritic segments (Figure 5F2); these were largely absent on control Purkinje cells at this stage (Figure 5E2). To quantify these effects, we categorized imaged Purkinje cells as having 1-2 primary dendrites or 3+ primary dendrites and, independently, as "spiny" or "non-spiny," blind to genotype and GluD2 level. 81% of controls at P7 had 1-2 primary dendrites, whereas only 35% of GluD2 OE cells had 1–2 primary dendrites (Figure 5G). Furthermore, although all control cells were non-spiny, 92% of GluD2 OE cells with 3+ primary dendrites were spiny (Figure 5H). The minority of non-spiny GluD2 OE cells tended to have lower GluD2 levels than the more typical spiny cells (Figure 5D). These









results suggest that GluD2 OE promotes Purkinje cell synaptogenesis with accompanying exuberant dendritic branching.

To test whether these early phenotypes persist in more mature Purkinje cells, we examined GluD2 OE Purkinje cells at P21. Strikingly, some GluD2 OE Purkinje cells had exuberant dendritic branches in the deep molecular layers but failed to extend branches to the pial surface (Figure 5I). These cells also had supernumerary primary dendrites (Figure 5J). Although control Purkinje cells had developed well-spaced dendritic spines by this stage (Figure 5K), in GluD2 OE Purkinje cells, individual dendritic protrusions were no longer easily resolved, and dendritic trunks appeared thicker, suggesting supernumerary dendritic spines (Figure 5L). We took an unbiased approach to quantifying these effects by imaging randomly selected transfected cells and then categorizing them based on their number of primary dendrites and, independently, their spine morphology (normal versus "hyper-spiny"), blind to genotype and GluD2 level. Of the 35 cells we quantified, all 7 cells with 3+ primary dendrites came from the GluD2 OE group (with 11 ± 2.4 primary dendrites; mean ± SEM). Furthermore, although all control cells and 95% of GluD2 OE cells with 1-2 primary dendrites had normal dendritic spines, 88% of GluD2 OE cells with 3+ primary dendrites exhibited the hyper-spiny phenotype (Figure S5A). Finally, cells with the supernumerary primary dendrite phenotype had higher levels of GluD2 OE (Figure 5M; see Figure S5B for representative images of Purkinie cells and their GluD2 intensities). Examination of GluD2 OE cells from unselected samples and additional samples selected based on their failure to reach the pial surface revealed that Purkinje cells with shorter dendritic trees also had very high levels of GluD2 OE, supernumerary primary dendrites, and increased thickness in the plane orthogonal to the plane of Purkinje cell dendrite elaboration (Figures S5C-S5E).

In MADM cerebella, sparse GluD2+/+ cells in an otherwise GluD2+/- background (Figure S2A) can also be considered cells with GluD2 OE relative to their neighbors. Interestingly, these GluD2<sup>+/+</sup> MADM OE cells also exhibited dendritic over-branching in the deep molecular layer (Figures 5N, 5O, and S5F; quantified in Figure 5P). The distribution of dendrite length within each bin, total number of branchpoints, and total dendrite length were not affected (Figures 5Q-5S).

These data indicate that GluD2 OE causes morphological phenotypes opposite to GluD2 sKO (Figure 5T): over-branching in the deep molecular layer and, in extreme cases, failure to extend dendritic branches to the superficial molecular layer altogether.

# GluD2 that does not bind Cbln1 cannot rescue the GluD2 sKO phenotypes

To test whether GluD2's interactions with its ligand Cbln1 are required for proper dendrite morphogenesis, we established an in vivo structure-function assay. The OE studies indicated that the gain-of-function phenotypes of GluD2 are expression level dependent (Figure 5D), as low levels of IUE-based GluD2 OE did not cause overt dendrite morphogenesis phenotypes. Thus, we used mild expression of wild-type GluD2 to rescue GluD2 sKO phenotypes by co-electroporating a plasmid encoding wild-type GluD2 (Figure 6A). We then compared this to the effect of expressing, at similar levels, a mutant GluD2 containing four point mutations (D24A, I26A, E61A, and R345A [GluD2DIER]; Figure 6B) that abolish binding to Cbln1 (Elegheert et al., 2016; Figures S6A-S6C).

Expression of the GluD2WT construct successfully rescued the GluD2 sKO branching and length distribution phenotypes (Figures S6D and S6E). Compared with wild-type GluD2 (GluD2WT) rescue Purkinje cells (Figure 6C; Figure S6F), GluD2DIER rescue Purkinje cells (Figures 6D and S6G) exhibited significantly fewer dendritic branches and reduced dendrite length in the deep molecular layer (quantified in Figures 6E and 6F). Total branch points and length did not differ significantly between these two conditions (Figures 6G and 6H). These results support the notion that dendritic branching defects caused by GluD2 sKO result from a disruption of signaling mediated by Cbln1-GluD2 interactions.

# Dendritic morphology phenotypes of GluD2 sKO are suppressed by loss of CbIn1

Our data thus far suggest that Cbln1-GluD2 signaling-mediated competition between neighboring Purkinje cells regulates dendritic branching. If so, then complete loss of Cbln1 should remove such competition and suppress the GluD2 sKO phenotypes.

To test this prediction, we combined Cbln1 KO with GluD2 sKO. To simplify genetic crosses, we developed a CRISPR-Cas9-based GluD2 sKO approach using plasmids expressing Cas9 and short guide RNAs (sgRNAs) against GluD2, along

#### Figure 4. GluD2 sKO phenotypes arise early and persist into adulthood

(A) Schematic time course of cerebellar development. EGL, external granular layer; IGL, internal granular layer.

(B) Schematic for genetically accessing Purkinje cells in Ai14 and GluD2<sup>fl/fl</sup>;Ai14 embryos.

(C and D) Control Purkinje cells (C) exhibit similar levels of dendritic elaboration in the deep and superficial ML between P10 and P63. GluD2 sKO Purkinje cells (D) exhibit an inverted triangular shape beginning around P10 and persisting at P63. Arrowheads in (D1) indicate overextension of dendritic branches beyond the superficial border of the ML. Higher magnification of superficial portions of dendritic trees and traced images is shown in insets in (C4) and (D4), highlighting frequent dendritic branch crossover in sKO but not control cells.

(E and F) Quantification of the normalized number of branchpoints (E) and dendrite length (F) in each ML bin in control (blue) and GluD2 sKO (red) Purkinje cells at P10. P14. and P63 (see Figures 1E and 1F for P21).

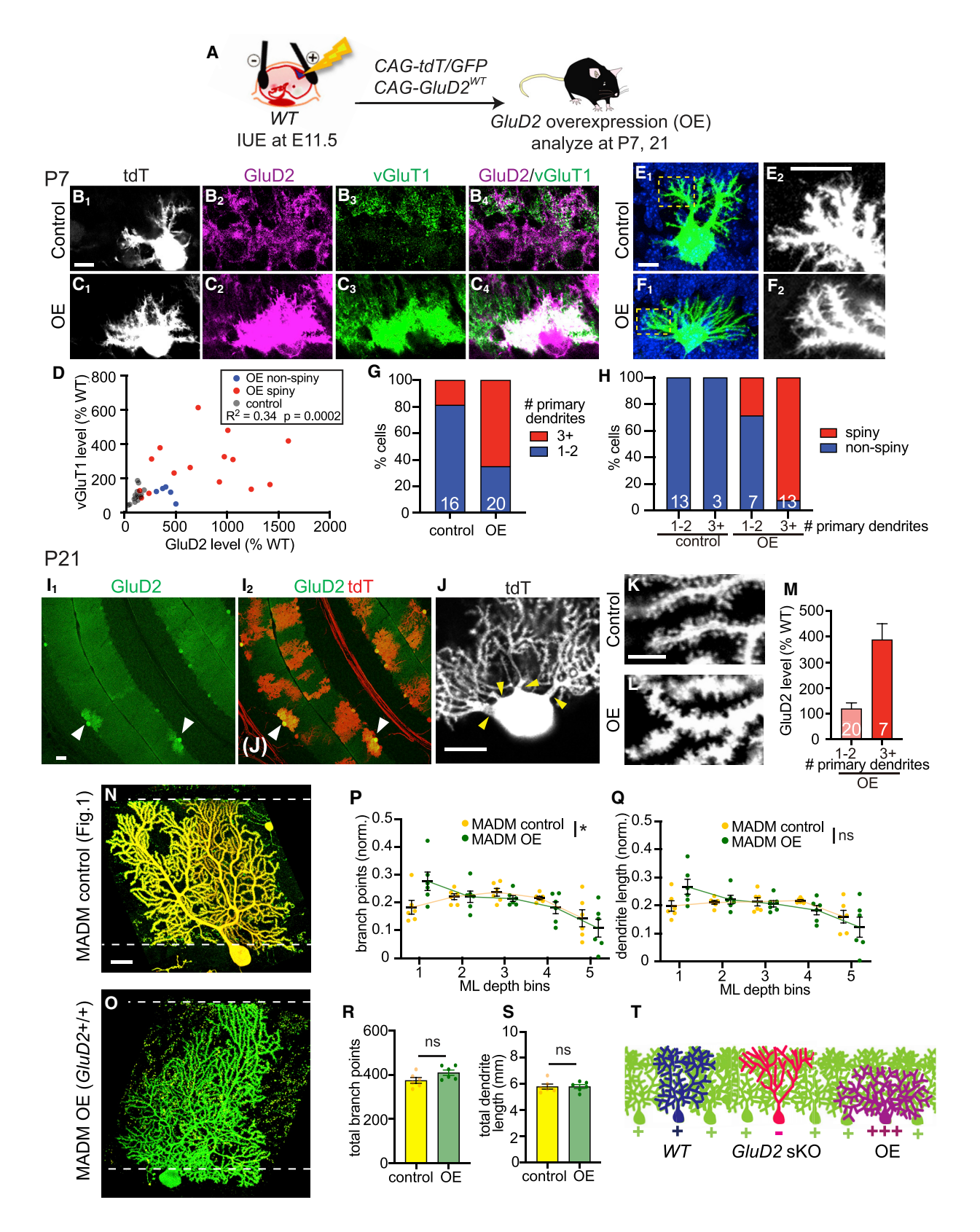
(G-I) Quantification of the total number of branchpoints (G), dendrite lengths (H), and average segment lengths (I) of control (blue) and GluD2 sKO (red) Pur-

(E-I) Data are mean ± SEM; n = 6, 6, 5, 5, 5, and 5 cells from 2, 2, 2, 2, and 4 mice for P10 control, P10 sKO, P14 control, P14 sKO, P63 control, and P63 sKO mice, respectively. P21 data are from Figure 1. \*p < 0.05, \*\*p < 0.01; ns, p > 0.05; two-way ANOVA (E and F) or t test (G-I).

(J) Representative tracings (from C<sub>4</sub> and D<sub>4</sub>) of P63 control and GluD2 sKO Purkinje cell dendritic arbors, with dendritic segments longer than 30 µm highlighted

Scale bars, 20 µm. See also Figure S4.









with GFP as a marker for IUE (Figure 7A; STAR methods). GluD2 staining validated loss of GluD2 expression in *GluD2* CRISPR-based sKO (*GluD2* csKO) cells but not in control cells with sgRNAs against *lacZ* (Figures S7A–S7D). When introduced into Purkinje cells in WT mice, *GluD2* csKO caused phenotypes (Figures 7B, 7C, S7E, and S7F) similar to those produced by IUE of Cre into *GluD2* fl/fl mice (Figures 1C and 1D) or MADM (Figures 1I and 1J). Quantification revealed fewer dendritic branchpoints and reduced dendrite length in the deep molecular layer and more dendritic branchpoints and increased length in the superficial layer compared with controls (Figures 7F and 7G). However, *GluD2* csKO in Purkinje cells of *Cbln1*-/- mice no longer exhibited the typical sKO dendrite branching phenotypes (Figures 7D, 7E, S7G, and S7H; quantified in Figures 7H and 7I).

Quantification across the entire dendritic tree revealed that loss of *Cbln1* did not affect total dendritic branchpoints and length (Figures 7J and 7K). *GluD2* csKO reduced dendritic branchpoints in WT mice (Figure 7J), consistent with IUE- and MADM-mediated sKO data (Figures 1G and 1M). Curiously, this phenotype persisted in *Cbln1*<sup>-/-</sup> mice (Figure 7J), suggesting that GluD2 may have a Cbln1-independent effect of promoting dendritic branching.

These experiments demonstrate that the altered dendritic branch distribution of *GluD2* sKO Purkinje cells requires the presence of Cbln1 and support the notion that Cbln1/GluD2-mediated competitive synaptogenesis between neighboring Purkinje cells underlies the dendrite morphological defects exhibited in *GluD2* sKO cells.

# A generative model recapitulates key aspects of Purkinje cell dendrite morphogenesis

To better understand the dynamics of dendrite growth and the consequences of *GluD2* manipulation, we developed a generative model of Purkinje cell dendrite morphogenesis. Because of the competitive nature of *GluD2*'s influence on dendrite growth,

we first modeled the growth of three adjacent WT Purkinje cells. This model uses nodes on a 2D lattice to represent synapses with parallel fibers, where occupied nodes indicate an existing synapse and unoccupied nodes indicate the potential for a synapse at that location (Figure 8A). Elongation extends an existing branch, whereas branching generates a new dendritic process that forks off of an existing branch. At every point in time and at each location in the dendritic arbor, the probabilities of elongation and branching are determined by three factors: (1) cellautonomous drives to elongate and branch that lessen as the total number of synapses on the tree increases; (2) repulsion from other dendritic processes in the vicinity of the node (Figure 8B); and (3) a force that attracts new dendrite growth upward toward the pial surface. The model iterates through each eligible node in the tree and makes the decision to elongate, branch, or neither based on these probabilities (Figure 8C). New parallel fibers progressively enter the simulation over time to model the developmental trajectory of the molecular layer (see STAR methods for details). WT cells, grown as described, tile the 2D grid and display a distinctly square-like morphology (Figures 8D and S8A: Video S1).

To simulate *GluD2* KO conditions, we reduced the ratio of a cell's drive to branch relative to its drive to elongate. This simulates decreased efficacy in stabilizing new synaptic partners and is based on our findings of reduced branching in the deep molecular layer (Figures 1F and 4E) and over-extension of dendritic branches beyond the upper border of the molecular layer in the initial stages of growth (Figures 4D and S4J). We also modified the growth parameters to mimic a reduction in synaptogenesis of *GluD2* KO cells compared with WT cells (Ichikawa et al., 2016).

We simulated sKO by only "mutating" the middle cell and observed an inverted triangular morphology like that of sKO cells (Figures 8E and S8B; Video S2). Analysis of time-lapse sequences (Video S2; Figure 8H) indicated that mutant cells

# Figure 5. GluD2 OE causes dendrite overelaboration in the deep ML

(A) Schematic of IUE for overexpressing GluD2 in WT mice.

(B and C) tdTomato (tdT) expression (B<sub>1</sub> and C<sub>1</sub>), immunostaining for GluD2 (B<sub>2</sub> and C<sub>2</sub>) and vGluT1 (B<sub>3</sub> and C<sub>3</sub>), and merge (B<sub>4</sub> and C<sub>4</sub>) in control (B) and GluD2 OE (C) Purkinje cells at P7. Scale bar, 10  $\mu$ m.

(D) Relationship between vGluT1 and GluD2 levels of each P7 control and GluD2 OE cell (dot).

(E and F) Representative images of control ( $E_1$ ) and GluD2 OE ( $F_1$ ) P7 Purkinje cells, showing supernumerary primary dendrites on the GluD2 OE cell. Blue, DAPI. ( $E_2$ ) and ( $F_2$ ) are high-magnification images of distal dendrites of ( $E_1$ ) and ( $F_1$ ) (boxed regions), showing many spine-like processes in GluD2 OE but not control cells. Scale bars, 10  $\mu$ m.

(G) Percentage of control and GluD2 OE cells with 1-2 or 3+ primary dendrites. The numbers of cells in each category are indicated.

(H) Percentage of spiny and non-spiny cells according to genotype and number of primary dendrites. The numbers of cells in each category are indicated.

(D, G, and H) n = 16 cells from 2 mice (control) and 20 cells from 2 mice (OE).

(I) Low-magnification images of a P21 cerebellar cortex showing GluD2 expression levels ( $I_1$ ) of cells transfected by IUE that are also labeled by tdT ( $I_2$ ). Arrowheads indicate two Purkinje cells with high levels of GluD2 OE and shorter dendritic trees. Scale bar, 50  $\mu$ m.

(J) Representative images of a GluD2 OE cell with multiple primary dendrites (arrowheads in I₂). Scale bar, 20 μm.

(K and L) High-magnification confocal images showing dendritic spines in control (K) and GluD2 OE (L) dendritic segments. Scale bar, 5 μm.

(M) GluD2 OE level according to the number of primary dendrites of P21 GluD2 OE cells (n = 27 cells from 2 mice) with 1–2 or 3+ primary dendrites. Data are mean ± SEM; the numbers of cells in each category are indicated.

(N and O) Representative confocal images of P21 MADM control (GluD2\*/-) and MADM OE (GluD2\*/-) cells. Scale bar, 20 µm.

(P and Q) Quantification of the normalized number of branchpoints (P) and dendrite length (Q) in each ML bin for control (yellow) and MADM OE (green) Purkinje cells. \*p < 0.05: ns. p > 0.05: two-way ANOVA.

(R and S) Quantification of the total number of branchpoints (R) and dendrite lengths (S) of control and MADM OE Purkinje cells.

(P-S) Data are mean  $\pm$  SEM; ns, p > 0.05; t test. n = 6 (GluD2+/- control) and 6 (GluD2+/- OE) cells from 2 mice.

(T) Schematic comparing WT, GluD2 sKO, and GluD2 OE dendritic trees.

See also Figure S5.

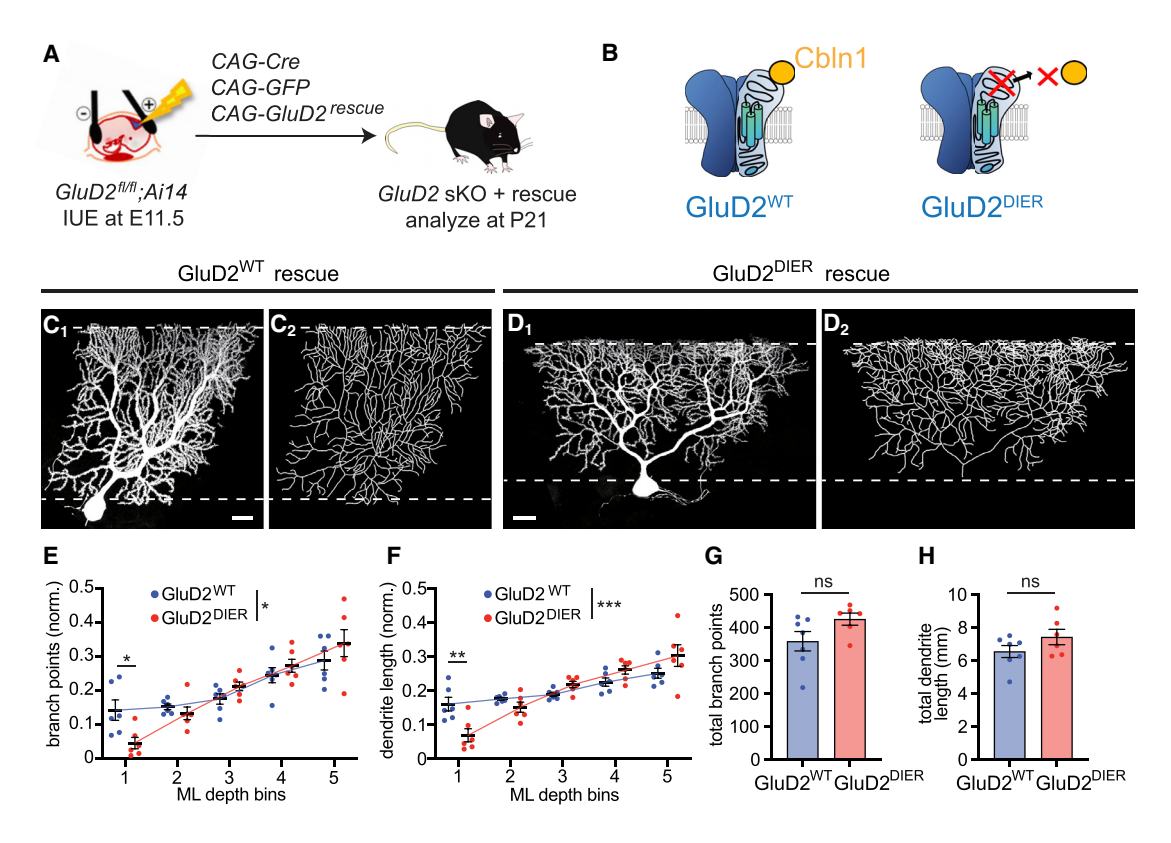


Figure 6. GluD2 that does not bind Cbln1 cannot rescue the GluD2 sKO phenotypes

(A) Schematic of the GluD2 rescue assay.

(B) Schematic showing that GluD2<sup>DIER</sup> (with four point mutations) does not bind the GluD2 ligand Cbln1.

(C and D) Confocal image (C<sub>1</sub> and D<sub>1</sub>) and tracing (C<sub>2</sub> and D<sub>2</sub>) of a representative GluD2 sKO Purkinje cell expressing a GluD2<sup>WT</sup> (C) or GluD2<sup>DIER</sup> (D) rescue construct. Scale bars, 20 µm.

(E and F) Quantification of the normalized number of branchpoints (E) and dendrite length (F) in each ML bin.

(G and H) Quantification of the total number of branchpoints (G) and dendrite length (H) of GluD2WT (blue) and GluD2DIER (red) rescue Purkinje cells.

Data from (E)–(H) are mean  $\pm$  SEM. n = 6 cells from 2 mice for each condition; \*p < 0.05, \*\*p < 0.01, \*\*\*p < 0.001; ns, p > 0.05; two-way ANOVA (between genotype) followed by Sidak's multiple comparisons tests between GluD2<sup>WT</sup> rescue and GluD2<sup>DIER</sup> rescue values in each bin (C and D) or t test (G and H). See also Figure S6.

extended fewer branches in the deep molecular layer than neighboring WT cells but reached the superficial molecular layer first and extended laterally before WT dendrites. Quantification of the final dendritic trees showed fewer dendritic branchpoints and reduced length in the deep molecular layers (Figures 81 and 8J). The total dendritic length in the superficial molecular layer was also increased in simulated sKO cells compared with controls (Figure 8J), but the over-branching phenotype in the superficial molecular layer was less pronounced (Figure 8I). These differences with experimental data may be due to our simulated dendritic trees growing exclusively in a single plane, whereas GluD2-deficient cells exhibited increased branching in and out of the dendritic plane, likely accounting for the dendritic branch crossings in the superficial layers of sKO cells (Figure 1F; Figure 4F3, inset). Simulating GluD2 OE by "mutating" the middle cell in the opposite direction as sKO recapitulated the "failure to reach the pial surface" phenotype but not the dendritic over-branching phenotypes (Figures 8G and S8D), also likely because of the 2D constraint of our model.

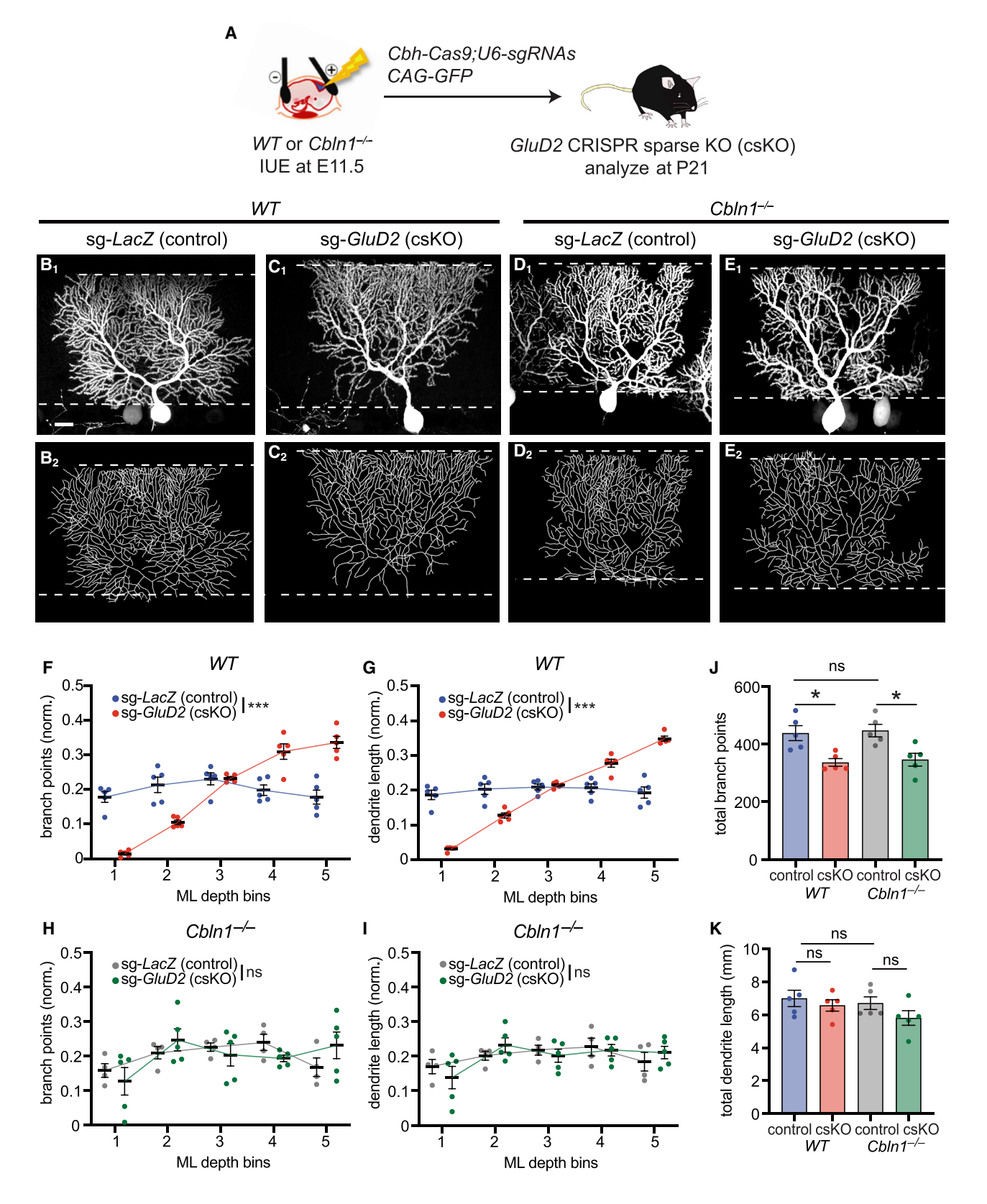
When we mutated all three cells in the 2D grid to simulate gKO conditions, all cells maintained a square-like morphology like that of WT cells (Figures 8F and S8C; Video S3; quantified in Figures 8K and 8L). Thus, these simulations recapitulated key features of GluD2 sKO and gKO cells, supporting the competitive nature of GluD2's effects on dendritic morphogenesis.

# **DISCUSSION**

Here we explore the relationship between synaptogenesis and dendrite morphogenesis by examining the effects of disrupting GluD2, a postsynaptic receptor required for synapse formation and maintenance, on dendrite morphology of cerebellar Purkinje cells. Several lines of evidence support the notion that the dendrite morphogenesis defects of GluD2 sKO cells were due to disruption of its established function in synapse formation and maintenance. (1) We observed, in GluD2 sKO cells, prevalence of thin filopodium-like protrusions in place of mature dendritic spines at P21 (Figures 2A-2C) and invasion of climbing fibers onto distal dendritic branches (Figure S3), consistent with disrupted parallel fiber → Purkinje cell synaptogenesis. (2) GluD2 sKO cells were apposed to less vGluT1 signal than control cells (Figures 2D-2I), indicating relative inability to attract









presynaptic partners. (3) GluD2 OE in Purkinje cells recruited more vGluT1 signal and produced more filopodial protrusions at P7 (Figure 5), consistent with GluD2's role in promoting synapse formation with parallel fibers. (4) GluD2 rescue required the ability to bind its ligand Cbln1 (Figure 6). (5) Dendrite morphogenesis phenotypes of GluD2 sKO cells were suppressed by concurrent loss of Cbln1 (Figure 7), suggesting that they were caused by neighboring Purkinje cells competing to form synapses with parallel fibers. (6) By simulating a synaptogenesis defect in a competitive dendrite growth model, we largely recapitulated GluD2 sKO and gKO morphological phenotypes (Figure 8), suggesting that reducing synaptogenesis in a competitive environment is sufficient to cause the dendrite morphogenesis defects we observed. Nevertheless, we cannot formally rule out the possibility that Cbln1-GluD2 interactions have a so far unidentified function unrelated to synaptogenesis that also contributes to the observed phenotypes.

GluD2 sKO Purkinje cells feature two prominent and countervailing characteristics: under-elaboration of the dendritic tree in the deep molecular layer and overelaboration in the superficial molecular layer (Figure 1). Morphological analyses across Purkinje cell postnatal development (Figure 4) reveal that the under-elaboration in the deep molecular layer coincides with reduced branching in the same locale, suggesting that the under-elaboration may be caused in part by a marked local reduction in dendritic branching. Without time-lapse imaging data, we cannot determine whether this is caused by a deficit in forming new branches or stabilizing newly formed branches. However, GluD2 OE caused supernumerary primary dendrites at P7, some of which persisted to P21 (Figure 5), suggesting that parallel fiber → Purkinje cell synaptogenesis may help stabilize dendritic branches. These phenotypes resemble those caused by perturbation of the neurexin/neuroligin synaptic organizers in Xenopus tectal neurons, where dendritic filopodia are destabilized by neuroligin disruption and stabilized by neuroligin OE (Chen et al., 2010). Indeed, the tripartite neurexin-Cbln1-GluD2 synaptic adhesion complex is believed to function in synaptogenesis in the cerebellum analogously to the neurexin-neuroligin complex elsewhere (Südhof, 2018; Yuzaki, 2017). Thus, just as in the Xenopus study (Chen et al., 2010), a reduction in dendritic branching of GluD2 sKO dendrites in the deep molecular layer supports the synaptotrophic hypothesis (Cline and Haas, 2008; Vaughn, 1989). We note, however, that, although global and sparse perturbations of neuroligin affect dendritic filopodium stability in Xenopus tectal neurons (Chen et al., 2010), the reduction of Purkinje cell dendritic branching in the deep molecular layer only occurs in GluD2 sKO cells, highlighting the importance of competition (English et al., 2012; Joo et al., 2014) in the regulation of Purkinje cell dendrite morphogenesis.

The overelaboration of Purkinje cell dendrites in the superficial molecular layer in GluD2 sKO cells appears to oppose the prediction of the synaptotrophic hypothesis and reveals a bimodal relationship between synaptogenesis and dendrite growth, echoing previous studies in Xenopus tectal neurons when manipulating effectors of synaptic transmission (Haas et al., 2006; Liu et al., 2009). We propose two explanations for this overelaboration phenotype. (1) Each Purkinje cell's dendrite growth may be homeostatically regulated by the total number of synapses formed with parallel fibers, which account for the vast majority of input synapses onto Purkinje cells. Under-elaboration of GluD2 sKO dendrites in the deep molecular layer may be compensated for by overelaboration in the superficial molecular layer to reach a set point of total synapses formed. (2) Formation of a stable synapse may signal to a dendritic growth cone to stop further exploration. By reducing the ability of Purkinje cell dendrites to form stable synapses with parallel fibers, GluD2 sKO may also prevent growth cessation, causing exuberant branching and dendritic over-extension. This is supported by our observation of preferential enrichment of long terminal segments in P63 mice (Figures 4I and 4J). These two explanations are not mutually exclusive; synapse formation as a signal to stop further dendritic exploration could be a mechanism underlying homeostatic regulation. Our generative model contains both elements, featuring the assumption that an increase in the number of synapses in a dendritic tree results in a homeostatic decrease in the drive for a tree to branch, like a signal to reduce further exploration, and such modeling yielded results similar to our experimental observations (Figure 8). To our knowledge, this is the first generative model of dendrite growth across development, which likely applies only to dendrites that tile and grow in a 2D plane.

Interestingly, the under-elaboration and overelaboration phenotypes were observed only via sKO but not gKO of GluD2. We expect that neighboring WT Purkinje cells would alter their dendrite morphology to tile the space as seen in our simulation (Figure 8H; Video S2), although, because of technical limitations, we could not validate this experimentally. These findings resemble those of our previous study of neurotrophin-3 (NT3)/ TrkC signaling, in which sKO but not gKO of the neurotrophin receptor TrkC caused a marked reduction in Purkinje cell dendrite length and branching (Joo et al., 2014). TrkC has been implicated as a synaptogenic receptor in hippocampal and cortical neurons

# Figure 7. GluD2 sKO phenotypes are blocked by loss of Cbln1

(A) Schematic of CRISPR-mediated sparse control (LacZ) or GluD2 sKO in Purkinje cells of WT or CbIn1<sup>-/-</sup> mice.

(B and C) Confocal image (B<sub>1</sub> and C<sub>1</sub>) and tracing (B<sub>2</sub> and C<sub>2</sub>) of a representative WT Purkinje cell expressing Cas9 and sgRNAs against LacZ (sg-LacZ [control], B) or GluD2 (sg-GluD2 [csKO], C).

(D and E) Same as (B) and (C) except in Cbln1-/- mice.

(B-E) Scale bars, 20 μm.

(F-I) Quantification of the normalized number of branchpoints (F and H) and dendrite length (G and I) of Purkinje cell dendrites in each ML bin in control (sg-LacZ: WT, blue; Cbln1-/-, gray) and GluD2 csKO (sg-GluD2: WT, red; Cbln1-/-, green) in WT (F and G) or Cbln1-/- (H and I) animals.

(J and K) Quantification of the total number of branchpoints (J) and dendrite length (K) of sg-LacZ/WT, sg-GluD2/WT, sg-LacZ/ Cbln1<sup>-/-</sup>, and sg-GluD2/ Cbln1<sup>-/-</sup> cells.

 $Data from (F)-(K) are mean \pm SEM; n = 5 cells from 2 mice for each condition; ***p < 0.001, *p < 0.005, two-way ANOVA (F-I) or one-way ANOVA followed by Sidak's and the second state of the second state of$ multiple comparisons test (J and K). See also Figure S7.



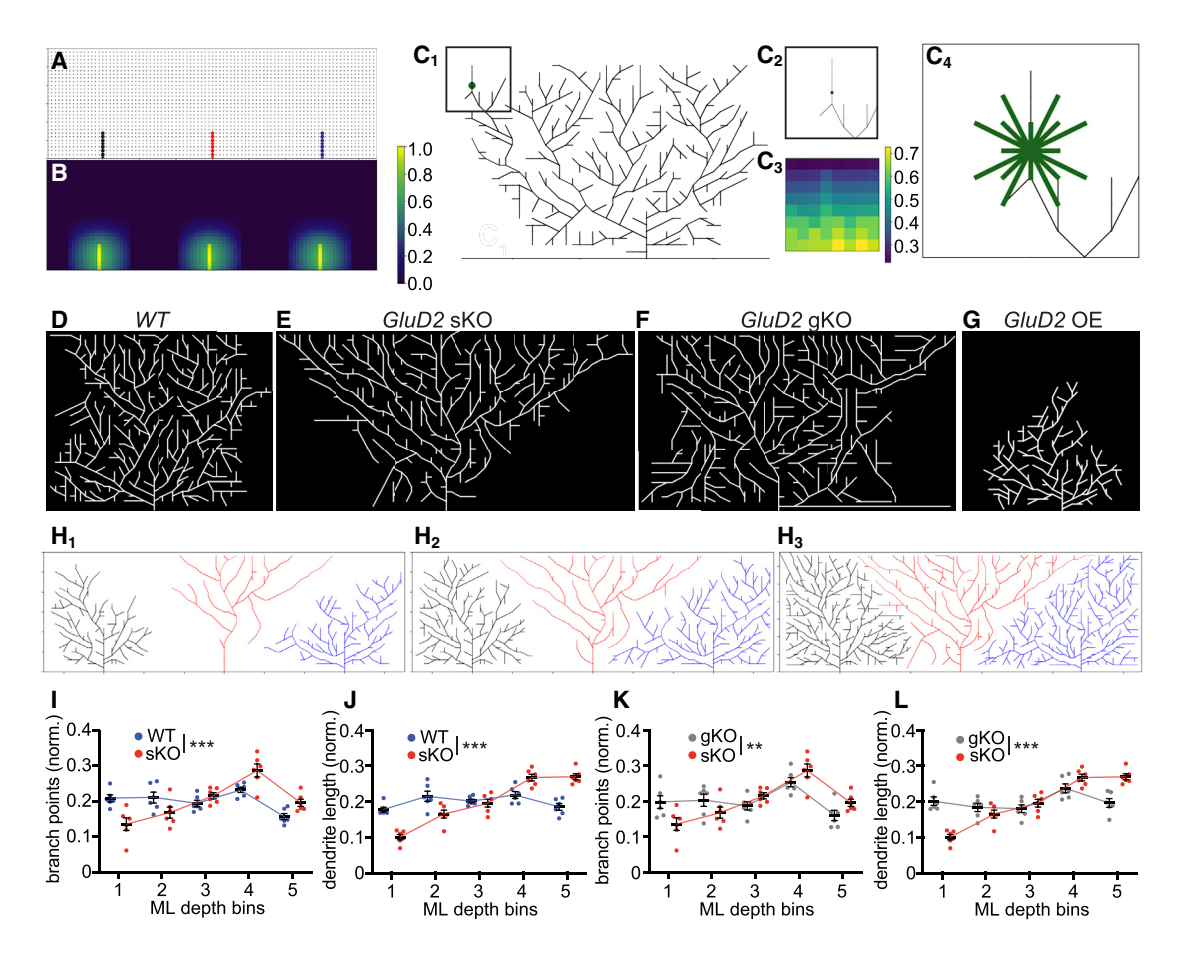


Figure 8. A generative model recapitulates key aspects of experimental data

(A) Skeleton of trees with which the model begins. Each node, denoted by a circle and representing a parallel fiber, is marked as occupied when the tree extends a branch through that point on the 2D lattice. This branch (edge) is indicated by a solid line, and the color of the line indicates to which tree the edge belongs (black, red, and blue for the left, center, and right tree, respectively). Other potential nodes for synapses are marked in gray. Occupied nodes contribute to repulsion felt in that part of the grid (STAR methods).

- (B) Heatmap of repulsion throughout the 2D grid shown in (A), with brighter colors indicating stronger repulsion, which discourages growth. For a given cell, the repulsion from nodes occupied by neighboring cells are stronger than repulsion from nodes occupied by itself. The color bar indicates the amount of repulsion normalized to the largest value of repulsion in this heatmap.
- (C) Example of a decision a cell might make about whether to branch from a certain point, with eligible directions of branching indicated.
- (C1) A Purkinje cell with a decision point for branching denoted by the green circle. The color bar indicates the amount of repulsion normalized to the largest value of repulsion in this heatmap.
- $(C_2)$  The vicinity of the green node shown in  $(C_1)$ .
- (C<sub>3</sub>) A heatmap of the repulsion around the green node, which determines the probability of branching in each direction.
- (C<sub>4</sub>) Eligible directions for branching from the central node marked by green edges. Note that some of these directions will have 0 probability of branching when they result in crossings with current branches, but all are pictured. The endpoint for each direction is determined by the closest lattice point in that direction; because this introduces different lengths, the probabilities of branching in longer directions are adjusted accordingly.
- (D) Representative example of a simulation with three WT Purkinje cells, showing the middle cell only.
- (E) Representative example of a simulation with one GluD2 KO Purkinje cell and two neighboring WT cells on either side, showing the middle cell only. This mimics
- (F) Representative example of a simulation with three GluD2 KO Purkinje cells, showing the middle cell only. This mimics the qKO condition.
- (G) Representative example of a simulation with one GluD2 OE Purkinje cell and two neighboring WT cells on either side, showing the middle cell only. This mimics the OE condition.
- (H<sub>1</sub>-H<sub>3</sub>) In-progress simulation at iteration 600 (H<sub>1</sub>), 800 (H<sub>2</sub>), and 1,400 (H<sub>3</sub>) with one GluD2 KO Purkinje cell (red) and two neighboring WT cells on either side (black and blue). Note that there is an expansion step between iteration 800 (H<sub>2</sub>) and 1,400 (H<sub>3</sub>).
- (I and J) Mean (±SEM) normalized dendritic branchpoints (I) and length (J) of bins in the ML for WT (blue) and GluD2 sKO (red) conditions.
- (K and L) Mean (±SEM) normalized dendritic branchpoints (I) and length (J) of bins in the ML for sKO (red) and gKO (gray) conditions.
- (I–L) Data are mean  $\pm$  SEM; n = 6 for all three conditions; \*\*p < 0.01, \*\*\*p < 0.001, two-way ANOVA.

See also Figure S8 and Videos S1, S2, and S3.

# **Neuron Article**



(Takahashi et al., 2011); however, evidence suggests that the effect of TrkC sKO in dendrite morphogenesis is distinct from its function as a synaptogenic receptor. The synaptogenic role of TrkC is independent of its NT3-binding and kinase activities (Takahashi et al., 2011), whereas TrkC's role in regulating Purkinje cell dendrite morphogenesis requires its kinase activity and interaction with NT3 (Joo et al., 2014). Furthermore, unlike GluD2 sKO, TrkC sKO causes a global decrease in dendritic branching and length. If the homeostasis hypothesis described above is true, then loss of NT3/TrkC may disrupt homeostasis, whereas loss of Cbln1/GluD2 may selectively affect morphological mechanisms downstream of competitive synaptogenesis without perturbing homeostatic regulation. While further exploration of the relationship between NT3/TrkC signaling and Cbln1/GluD2 signaling will enrich our understanding of the mechanisms of dendrite morphogenesis, both studies highlight the competitive nature of dendrite morphogenesis in mammalian central nervous system neurons and reinforce the importance of studying dendrite development using mosaic methods such as IUE and MADM.

#### **STAR**\*METHODS

Detailed methods are provided in the online version of this paper and include the following:

- KEY RESOURCES TABLE
- RESOURCE AVAILABILITY
  - Lead contact
  - Materials availability
  - Data availability
- EXPERIMENTAL MODEL AND SUBJECT DETAILS
  - Mice
- METHOD DETAILS
  - In utero electroporation (IUE)
  - Cloning and Plasmids
  - Histology and image acquisition
  - Antibodies
  - Image analysis and processing
  - O Evaluating baseline parameters for controls
- QUANTIFICATION AND STATISTICAL ANALYSIS
  - MODELING AND SIMULATION METHODS

#### SUPPLEMENTAL INFORMATION

Supplemental Information can be found online at https://doi.org/10.1016/j. neuron.2020.11.028.

#### **ACKNOWLEDGMENTS**

We thank M. Mishina for GluD2<sup>fl</sup> frozen embryos; T.C. Südhof and J.I. Morgan for Cbln1<sup>fl</sup> mice; L. Anderson for help with generating the MADM alleles; W. Joo for a previously unpublished construct: M. Yuzaki, K. Shen, J. Ding, and members of the Luo lab, including J.M. Kebschull, H. Li, J. Li, T. Li, C.M. McLaughlin, D. Pederick, J. Ren, D.C. Wang, and C. Xu, for discussions and critique of the manuscript; and M. Yuzaki for supporting Y.H.T. during the final phase of this project. Y.H.T. was supported by a JSPS fellowship. S.A.S. and L.J. were supported by Stanford graduate fellowships and NSF predoctoral fellowships. M.J.W. was supported by a Burroughs Wellcome Fund CASI award. This work was supported by NIH grant R01-NS050538 (to L.L.) and the European Research Council under the European Union Horizon 2020 Research and Innovations Program (725780 LinPro to S.H). S.G. thanks the Simons Foundation, James S. McDonnell Foundation, and NSF CAREER for support. L.L. is an HHMI investigator.

#### **AUTHOR CONTRIBUTIONS**

Y.H.T., S.A.S., and L.L. designed the experiments. Y.H.T. carried out IUE experiments with help from D.J.L. and S.A.S. S.A.S. made the DNA constructs. Y.H.T. and S.A.S. performed histology and data analyses with assistance from M.H. L.J. performed the simulation with guidance from M.J.W. and S.G. T.R., X.C., and S.H. provided unpublished MADM mice. Y.H.T., S.A.S., L.J., and L.L. wrote the manuscript with feedback from all authors. L.L. supervised the project.

#### **DECLARATION OF INTERESTS**

The authors have no competing interest.

Received: June 16, 2020 Revised: September 21, 2020 Accepted: November 25, 2020 Published: December 21, 2020

#### REFERENCES

Altman, J. (1972a). Postnatal development of the cerebellar cortex in the rat. I. The external germinal layer and the transitional molecular layer. J. Comp. Neurol. 145, 353-397.

Altman, J. (1972b). Postnatal development of the cerebellar cortex in the rat. II. Phases in the maturation of Purkinje cells and of the molecular layer. J. Comp. Neurol. 145, 399-463.

Bosman, L.W.J., and Konnerth, A. (2009). Activity-dependent plasticity of developing climbing fiber-Purkinje cell synapses. Neuroscience 162, 612-623. Chen, S.X., Tari, P.K., She, K., and Haas, K. (2010), Neurexin-neuroligin cell

adhesion complexes contribute to synaptotropic dendritogenesis via growth stabilization mechanisms in vivo. Neuron 67, 967-983.

Cline, H., and Haas, K. (2008). The regulation of dendritic arbor development and plasticity by glutamatergic synaptic input: a review of the synaptotrophic hypothesis. J. Physiol. 586, 1509-1517.

Contreras, X., Davaatseren, A., Amberg, N., Hansen, A.H., Sonntag, J., Andersen, L., Bernthaler, T., Heger, A., Johnson, R., Schwarz, L.A., et al. (2020). A Genome-wide Library of MADM Mice for Single-Cell Genetic Mosaic Analysis. bioRxiv. https://doi.org/10.1101/2020.06.05.136192.

Elegheert, J., Kakegawa, W., Clay, J.E., Shanks, N.F., Behiels, E., Matsuda, K., Kohda, K., Miura, E., Rossmann, M., Mitakidis, N., et al. (2016). Structural basis for integration of GluD receptors within synaptic organizer complexes. Science

English, C.N., Vigers, A.J., and Jones, K.R. (2012). Genetic evidence that brain-derived neurotrophic factor mediates competitive interactions between individual cortical neurons. Proc. Natl. Acad. Sci. USA 109, 19456-19461.

Espinosa, J.S., and Luo, L. (2008). Timing neurogenesis and differentiation: insights from quantitative clonal analyses of cerebellar granule cells. J. Neurosci. 28. 2301-2312.

Haas, K., Li, J., and Cline, H.T. (2006). AMPA receptors regulate experiencedependent dendritic arbor growth in vivo. Proc. Natl. Acad. Sci. USA 103,

Hashimoto, K., Ichikawa, R., Takechi, H., Inoue, Y., Aiba, A., Sakimura, K., Mishina, M., Hashikawa, T., Konnerth, A., Watanabe, M., and Kano, M. (2001). Roles of glutamate receptor δ 2 subunit (GluRdelta 2) and metabotropic glutamate receptor subtype 1 (mGluR1) in climbing fiber synapse elimination during postnatal cerebellar development. J. Neurosci. 21, 9701–9712.

Hirai, H., Pang, Z., Bao, D., Miyazaki, T., Li, L., Miura, E., Parris, J., Rong, Y., Watanabe, M., Yuzaki, M., and Morgan, J.I. (2005). Cbln1 is essential for synaptic integrity and plasticity in the cerebellum. Nat. Neurosci. 8, 1534–1541.





Ichikawa, R., Miyazaki, T., Kano, M., Hashikawa, T., Tatsumi, H., Sakimura, K., Mishina, M., Inoue, Y., and Watanabe, M. (2002). Distal extension of climbing fiber territory and multiple innervation caused by aberrant wiring to adjacent spiny branchlets in cerebellar Purkinje cells lacking glutamate receptor delta 2. J. Neurosci. 22, 8487-8503.

Ichikawa, R., Sakimura, K., and Watanabe, M. (2016). GluD2 Endows Parallel Fiber-Purkinje Cell Synapses with a High Regenerative Capacity. J. Neurosci. 36. 4846-4858.

Jan, Y.-N., and Jan, L.Y. (2010). Branching out: mechanisms of dendritic arborization. Nat. Rev. Neurosci. 11, 316-328.

Joo, W., Hippenmeyer, S., and Luo, L. (2014). Dendrite morphogenesis depends on relative levels of NT-3/TrkC signaling. Science 346, 626-629.

Kalb, R.G. (1994). Regulation of motor neuron dendrite growth by NMDA receptor activation. Development 120, 3063-3071.

Kaneko, M., Yamaguchi, K., Eiraku, M., Sato, M., Takata, N., Kiyohara, Y., Mishina, M., Hirase, H., Hashikawa, T., and Kengaku, M. (2011). Remodeling of monoplanar Purkinje cell dendrites during cerebellar circuit formation. PLoS ONE 6, e20108.

Kashiwabuchi, N., Ikeda, K., Araki, K., Hirano, T., Shibuki, K., Takayama, C., Inoue, Y., Kutsuwada, T., Yagi, T., Kang, Y., et al. (1995). Impairment of motor coordination, Purkinje cell synapse formation, and cerebellar long-term depression in GluR  $\delta$  2 mutant mice. Cell 81, 245–252.

Konno, K., Matsuda, K., Nakamoto, C., Uchigashima, M., Miyazaki, T., Yamasaki, M., Sakimura, K., Yuzaki, M., and Watanabe, M. (2014). Enriched expression of GluD1 in higher brain regions and its involvement in parallel fiber-interneuron synapse formation in the cerebellum. J. Neurosci. 34, 7412-7424

Kulkarni, V.A., and Firestein, B.L. (2012). The dendritic tree and brain disorders. Mol. Cell. Neurosci. 50, 10-20.

Kurihara, H., Hashimoto, K., Kano, M., Takayama, C., Sakimura, K., Mishina, M., Inoue, Y., and Watanabe, M. (1997). Impaired parallel fiber->Purkinje cell synapse stabilization during cerebellar development of mutant mice lacking the glutamate receptor δ2 subunit. J. Neurosci. 17, 9613–9623.

Liu, X.F., Tari, P.K., and Haas, K. (2009). PKM zeta restricts dendritic arbor growth by filopodial and branch stabilization within the intact and awake developing brain. J. Neurosci. 29, 12229-12235.

Maddalo, D., Manchado, E., Concepcion, C.P., Bonetti, C., Vidigal, J.A., Han, Y.C., Ogrodowski, P., Crippa, A., Rekhtman, N., de Stanchina, E., et al. (2014). In vivo engineering of oncogenic chromosomal rearrangements with the CRISPR/Cas9 system. Nature 516, 423-427.

Matsuda, T., and Cepko, C.L. (2004). Electroporation and RNA interference in the rodent retina in vivo and in vitro. Proc. Natl. Acad. Sci. USA 101, 16-22.

Matsuda, T., and Cepko, C.L. (2007). Controlled expression of transgenes introduced by in vivo electroporation. Proc. Natl. Acad. Sci. USA 104, 1027-1032.

Matsuda, K., Miura, E., Miyazaki, T., Kakegawa, W., Emi, K., Narumi, S., Fukazawa, Y., Ito-Ishida, A., Kondo, T., Shigemoto, R., et al. (2010). Cbln1 is a ligand for an orphan glutamate receptor delta2, a bidirectional synapse organizer. Science 328, 363-368.

Miyazaki, T., Fukaya, M., Shimizu, H., and Watanabe, M. (2003). Subtype switching of vesicular glutamate transporters at parallel fibre-Purkinje cell synapses in developing mouse cerebellum. Eur. J. Neurosci. 17, 2563-2572.

Niell, C.M., Meyer, M.P., and Smith, S.J. (2004). In vivo imaging of synapse formation on a growing dendritic arbor. Nat. Neurosci. 7, 254-260.

Nishiyama, J., Hayashi, Y., Nomura, T., Miura, E., Kakegawa, W., and Yuzaki, M. (2012). Selective and regulated gene expression in murine Purkinje cells by in utero electroporation. Eur. J. Neurosci. 36, 2867-2876.

Petersen, P.H., Zou, K., Hwang, J.K., Jan, Y.N., and Zhong, W. (2002). Progenitor cell maintenance requires numb and numblike during mouse neurogenesis. Nature 419, 929-934.

Südhof, T.C. (2018). Towards an understanding of synapse formation. Neuron 100, 276-293.

Takahashi, H., Arstikaitis, P., Prasad, T., Bartlett, T.E., Wang, Y.T., Murphy, T.H., and Craig, A.M. (2011). Postsynaptic TrkC and presynaptic PTP<sub>o</sub> function as a bidirectional excitatory synaptic organizing complex. Neuron 69, 287-303.

Takeo, Y.H., Kakegawa, W., Miura, E., and Yuzaki, M. (2015). Rorα regulates multiple aspects of dendrite development in cerebellar purkinje cells in vivo. J. Neurosci. 35, 12518-12534.

Takeuchi, T., Miyazaki, T., Watanabe, M., Mori, H., Sakimura, K., and Mishina, M. (2005). Control of synaptic connection by glutamate receptor delta2 in the adult cerebellum. J. Neurosci. 25, 2146-2156.

Uemura, T., Lee, S.-J., Yasumura, M., Takeuchi, T., Yoshida, T., Ra, M., Taguchi, R., Sakimura, K., and Mishina, M. (2010). Trans-synaptic interaction of GluRdelta2 and Neurexin through CbIn1 mediates synapse formation in the cerebellum, Cell 141, 1068-1079.

Vaughn, J.E. (1989). Fine structure of synaptogenesis in the vertebrate central nervous system. Synapse 3, 255-285.

West, M.J., and del Cerro, M. (1976). Early formation of synapses in the molecular layer of the fetal rat cerebellum. J. Comp. Neurol. 165, 137-153.

Yogev, S., and Shen, K. (2014). Cellular and molecular mechanisms of synaptic specificity. Annu. Rev. Cell Dev. Biol. 30, 417-437.

Yuzaki, M. (2017). The C1q complement family of synaptic organizers: not just complementary. Curr. Opin. Neurobiol. 45, 9-15.

Zong, H., Espinosa, J.S., Su, H.H., Muzumdar, M.D., and Luo, L. (2005). Mosaic analysis with double markers in mice. Cell 121, 479-492.



# **STAR**\***METHODS**

# **KEY RESOURCES TABLE**

REAGENT or RESOURCE	SOURCE	IDENTIFIER
Antibodies		
goat anti-GluD2	Santa Cruz Biotechnology	Cat# sc-26118; RRID:AB_2114046
goat anti-GluD2	Frontier Institute	RRID: AB_2571602
rabbit anti-HA	Cell Signaling Technology	Cat# 3724; RRID:AB_1549585
guinea pig anti-vGluT1	Millipore EMD	Cat# AB5905; RRID:AB_2301751
guinea pig anti-vGluT1	Frontier Institute	RRID: AB_2571602
guinea pig anti-vGluT2	Millipore EMD	Cat# AB2251-I; RRID:AB_2665454
guinea pig anti-vGluT2	Frontier Institute	RRID: AB_2571621
chicken anti-GFP	Aves Labs	Cat# GFP-1020; RRID:AB_2307313
rabbit anti-DsRed/tdTomato	Clontech/Takara Bio	Cat# 632496; RRID: AB_10013483
Alexa Fluor 488 Donkey Anti-Chicken IgY (IgG) antibody	Jackson ImmunoResearch Labs	Cat# 703-545-155; RRID:AB_2340375
Cy3 Donkey Anti-Rabbit IgG antibody	Jackson ImmunoResearch Labs	Cat# 711-165-152; RRID:AB_2307443
Alexa Fluor 647 Donkey Anti-Goat IgG antibody	Jackson ImmunoResearch Labs	Cat# 705-605-003; RRID:AB_2340436
DyLight 405 Donkey Anti-Rabbit IgG antibody	Jackson ImmunoResearch Labs	Cat# 711-475-152; RRID:AB_2340616
Alexa Fluor 647 Donkey Anti-Rabbit IgG antibody	Jackson ImmunoResearch Labs	Cat# 711-605-152; RRID:AB_2492288
Alexa Fluor 647 Donkey Anti-Guinea Pig IgG antibody	Jackson ImmunoResearch Labs	Cat# 706-605-148; RRID:AB_2340476
Alexa Fluor 488 Donkey Anti-Guinea Pig IgG antibody	Jackson ImmunoResearch Labs	Cat# 706-545-148; RRID:AB_2340472
Cy3 Donkey Anti-Guinea Pig IgG antibody	Jackson ImmunoResearch Labs	Cat# 706-165-148; RRID:AB_2340460
Chemicals, peptides, and recombinant proteins	Cacheer mindre recearch Labe	Cath 700 100 110, 111 112.11 12_20 10 100
soflurane	Henry Schein Animal Health	CAS# 26675-46-7; CHEBI:6015
Avertin (2,2,2-Tribromoethanol)	Sigma	SKU# T48402
DAPI	ThermoFisher Scientific	Cat# D1306
Fast Green dye	Millipore Sigma	Cat# F7258
Buprenorphine-SR	ZooPharm	lot # BSRLAB0.5-191112
Ritodrine hydrochloride	Sigma	R0758
Friton X-100	v	T8787
Fluoromount-G	Millipore Sigma ThermoFisher Scientific	Cat# 00-4958-02
normal donkey serum	Jackson ImmunoResearch Labs	Cat# 017-000-121; RRID:AB_2337258
Experimental models: organisms/strains		
Mouse: Crl:CD1(ICR)	Charles River	RRID:IMSR_CRL:022
Mouse: Ai14	JAX	JAX stock #007908; RRID: IMSR_JAX:007908
Mouse: GluD2-fl	Takeuchi et al., 2005	N/A
Mouse: Cbln1-fl	T.C. Sudhof/J.I. Morgan	N/A
Mouse: Hprt-Cre	JAX	JAX stock #004302; RRID: IMSR_JAX:004302
Mouse: Nestin-Cre8.5	Petersen et al., 2002	N/A
Mouse: MADM6-GT	Contreras et al., 2020	N/A
Mouse: MADM6-TG	Contreras et al., 2020	N/A
Dligonucleotides		
_acZ-sg1 target sequence: TGCGAATACGCCCACGCGAT	This paper	N/A
LacZ-sg2 target sequence: CGGCGCGTAAAAATGCGCTC	This paper	N/A
Grid2-sg1 target sequence: TGATAGAATCAGCGGTCGCC	This paper	N/A
Grid2-sg2 target sequence: CCTTCTGTTGGTCTCGAACC	This paper	N/A

(Continued on next page)





Continued		
REAGENT or RESOURCE	SOURCE	IDENTIFIER
Recombinant DNA		
pCAG-Cre	Matsuda and Cepko, 2007	RRID:Addgene_13775
pCAG-GFP	Matsuda and Cepko, 2004	RRID:Addgene_11150
pAAV-CAG-eGFP	E. Boyden, unpublished	RRID:Addgene_37825
pCAG-tdTomato	W. Joo	N/A
pCAG-2xHA-GluD2WT	This paper	N/A
pCAG-2xHA-GluD2-DIER	This paper	N/A
pX333	Maddalo et al., 2014	RRID:Addgene_64073
pX333-CBh-Cas9-U6-sgRNA-LacZ	This paper	N/A
pX333-CBh-Cas9-U6-sgRNA-GluD2	This paper	N/A
Software and algorithms		
ZEN	Carl Zeiss	RRID: SCR_013672
Imaris 9.3	Oxford Instruments	RRID:SCR_007370; https://imaris.oxinst.com/
ImageJ (Fiji)	NIH	https://imagej.net/Fiji/Downloads
Prism 8.4	GraphPad	RRID:SCR_002798; https://www. graphpad.com/
Excel	Microsoft	RRID:SCR_016137
Python	Python Software Foundation	https://www.python.org

#### RESOURCE AVAILABILITY

# **Lead contact**

Further information and requests for resources and reagents should be directed to and will be fulfilled by the Lead Contact, Liqun Luo (lluo@stanford.edu)

#### **Materials availability**

New plasmids will be deposited at Addgene. Other materials will be made available upon requests.

#### **Data availability**

All data have been presented in Figures and Supplemental Figures. Original images and modeling codes will be made available upon requests.

## **EXPERIMENTAL MODEL AND SUBJECT DETAILS**

All procedures followed animal care and biosafety guidelines approved by Stanford University's Administrative Panel on Laboratory Animal Care and Administrative Panel of Biosafety in accordance with NIH guidelines. Mice were housed in plastic cages with disposable bedding on a 12 hours light/dark cycle with food and water available ad libitum. Pregnant CD1 dams were ordered from Charles River. GluD2<sup>fl</sup> frozen embryos were a kind gift from M. Mishina. Cbln1<sup>fl</sup> mice were a kind gift from T.C. Südhof and were generated by J. Morgan.  $GluD2^{fl}$  mice and  $Cbln1^{fl}$  mice were crossed to  $Hprt^{Cre}$  mice obtained from The Jackson Laboratory to generate  $GluD2^{-l}$ (gKO) and Cbln1<sup>-/-</sup> mice, respectively. Ai14 mice were obtained from The Jackson Laboratory. Nestin-Cre8.5 mice were a kind gift from W. Zhong. MADM-mediated GluD2 sparse knockout mice were generated using MADM6<sup>GT</sup> and MADM6<sup>TG</sup> alleles (Contreras et al., 2020) assembled into MADM6-GluD2<sup>fl</sup> mice as previously described (Joo et al., 2014), with the Nestin-Cre8.5 transgene driving Cre expression in neural progenitor cells.

# **METHOD DETAILS**

#### In utero electroporation (IUE)

In utero electroporation into mouse cerebellar Purkinje cells was performed as described (Nishiyama et al., 2012) with some modifications. Embryonic day 11.5 (E11.5) pregnant dams were anesthetized by isoflurane (starting at 2.5% and maintained at 1.5% 1 L O<sub>2</sub>/min). After cleaning the abdomen with betadine, a laparotomy was performed, uterine horns were exposed, and DNA was injected within the following 20–30 minutes. To relax the myometrium, ritodrine hydrochloride (0.4–0.8 μg/g; Sigma-Aldrich, St Louis,



MO, USA) was injected into the abdominal cavity or directly onto the exposed uterine horns. Warm sterile PBS was continually applied to the embryos to hydrate them. Under the illumination of a fiber optic light source (Dolan Jenner) with a flexible light guide (Allied Electronics), a plasmid DNA solution in a glass capillary needle was injected into the fourth ventricle using a microinjector (Eppendorf FemtoJet 4l; Eppendorf) until the rostral region of the fourth ventricle was filled with DNA, as visualized with Fast Green dye (Sigma). The volume injected into each embryo was approximately 2-3 µL. After injection, the embryo was held through the uterus with tweezer-style electrodes (CUY650P3; NEPAGENE) so that the positive metal electrode was placed on the rostral rhombic lip of the fourth ventricle, and 1-2 sets of electrical pulses (33-38 V, each with a duration of 30 ms, five pulses at intervals of 970 ms per pulse) were delivered using an electroporater (ECM 399, BTX). After electroporation, the uterus was repositioned in the abdominal cavity, 0.05-0.10 mg/kg buprenorphine-SR was injected directly into the intraperitoneal space. The abdominal wall and skin were then sutured closed. The dams were kept on a heating pad until recovery from anesthesia, then returned to their home cages. The embryos were allowed to continue developing and were typically born on E19. After birth, pups were screened for successful electroporation by examining their cerebella through the skin and skull under a fluorescence stereomicroscope, then returned to their home cage with the dam.

For deleting GluD2 by introducing Cre into GluD2<sup>fl/fl</sup> mice, we used the Ai14 mouse line as the background. Because tdTomato (tdT) is also expressed sparsely in some cell types other than Purkinje cells (see below), in order to label single Purkinje cell morphology, we coelectroporated GFP with Cre. For Figures 1 and 4, we detected possible knockout cells by Cre-dependent expression of tdT from the Ai14 allele, and validated deletion of GluD2 by antibody staining. We found that all the imaged tdT/GFP-double positive Purkinje cells lacked GluD2 staining. Therefore, based on the assumption that most of tdT-positive Purkinje cells are GluD2 knockout, we analyzed tdT/GFP-double possitive Purkinje cells without staining GluD2 for sKO experiments in Figures 2D-2F and Figure S3B. The expression of plasmid genes by IUE is highly specific to the Purkinje cells (Nishiyama et al., 2012), because at the timing of IUE (E11.5), Purkinje cells are the majority of cells that have finished terminal differentiation by the rostral 4th ventricular zone. There is a chance that plasmids can be introduced in other cell types near the ventricular zone, but most of them are still progenitors and actively dividing, diluting the plasmids to the point the transgenes are no longer detectable. However, when Cre plasmids are electroporated, expression of Cre, even briefly, can activate recombination in such progenitor cells. For our experiments using Cre plasmids for IUE into Ai14 mice, some granule cells, molecular layer interneurons and radial glial cells are occasionally sparsely labeled by tdT but not by GFP. It is unlikely that sparse deletion of GluD2 (if it occurs) in such Cre-expressing non-Purkinje cells affects Purkinje cell dendrite morphology because (1) GluD2 is not expressed in granule cells and radial glial cells, and (2) while molecular layer interneurons express GluD2, they also express GluD1, which plays a more central role and can compensate for loss of GluD2 (Konno et al., 2014).

#### **Cloning and Plasmids**

Standard cloning procedures were used to generate new DNA constructs. GluD2 overexpression constructs had two hemagglutinin (HA) tags inserted immediately following the GluD2 signal sequence and followed by GSG linkers. GluD2 expression constructs were subcloned into a pCAG vector derived from pCAG-Cre (Addgene). The DIER mutant had four point mutations (D24 $\rightarrow$ A, I24 $\rightarrow$ A, E61 → A, R345 → A; Elegheert et al., 2016) that abolish binding to cerebellin-1 (Cbln1). Two independent sgRNAs were subcloned into the pX333 plasmid vector (Addgene) for CRISPR-mediated experiments (sgLacZ primer sequences: tgcgaatacgcccacgcgat, cggcgcgtaaaaatgcgctc; sgGluD2 primer sequences: tgatagaatcagcggtcgcc, ccttctgttggtctcgaacc).

Plasmid DNA for IUE was purified using the QIAGEN plasmid maxiprep kit (QIAGEN) and, following ethanol precipitation, dissolved in HEPES-buffered saline. The plasmid solutions were colored with 0.01% Fast Green so that they were visible when injected into the fourth ventricle. The plasmid DNA used for IUE and their final concentrations were as follows: 1 and 2 μg/μL for pCAG-eGFP (or pCAG-GFP) and pCAG-Cre, respectively (Figures 1, 2, and 4); 3 µg/µL for pCAG-eGFP or pCAG-tdTomato (pCAG-tdT) alone (Figures 3 and 5); 1 and 2  $\mu$ g/ $\mu$ L for pCAG-tdT and pCAG-tdA-tdCre and pCAG-HA-GluD2WT/pCAG-HA-GluD2DIER, respectively (Figure 6); and 1 and 2 μg/μL for pCAG-eGFP and pX333-CBh-Cas9-U6-sgRNA-LacZ/GluD2, respectively (Figure 7).

Typically, the rate of co-expression of multiple plasmids in Purkinje cells by IUE is usually very high (> 95%, see (Nishiyama et al., 2012). For example, for the cells shown in Figure 5I, 95.2% (20 out of 21 cells) of the tdTomato-positive cells were HA-positive (HA staining not shown), suggesting that most of the transfected Purkinje cells co-expressed both of the two plasmids electroporated.

# **Histology and image acquisition**

Mice were deeply anesthetized using 2.5% Avertin and perfused transcardially using 4% paraformaldehyde (PFA) in PBS. The fixed brains were dissected out and postfixed for 1-4 hours at room temperature or overnight at 4°C in 4% PFA in PBS. After washing in PBS, 100-µm thick sagittal cerebellar sections were collected from the cerebellar vermis using a vibratome (Leica), blocked in 10% normal donkey serum in 0.1% Triton X-100 in PBS, and incubated with primary antibodies overnight at room temperature or over two nights at 4°C. Sections were then washed in PBS three times, incubated with Alexa Fluor secondary antibodies (Jackson ImmunoResearch Laboratories) for at least 1 hour at room temperature, washed three times in PBS and mounted and coverslipped on glass slides using Fluoromount-G (Thermo Fisher Scientific). Sections were imaged using a Zeiss LSM 780 laser-scanning confocal microscope (Carl Zeiss).

The z stacked images for dendrite tracing were acquired using a 40 × /1.4 Plan-Apochromat oil immersion objective (Carl Zeiss), at 2048 × 2048 pixels per frame with 0.4 μm z-steps. For IUE-based experiments, Purkinje cells in the bank region of the cerebellar





primary fissure were imaged. For experiments using MADM mice, Purkinje cells in the bank regions of the cerebellar primary fissure and lobules III and IV were imaged.

To measure GluD2, vGluT1, and vGluT2 expression and image dendritic spines used in the unbiased analyses in Figure 5, an 20 x /0.8 Plan-Apochromat air immersion objective (Carl Zeiss) and an 40X/1.4 Plan-Apochromat oil immersion objective (Carl Zeiss) were used. Images in Figure 5I were collected using a 10X/0.3 Plan-Neofluar air immersion objective (Carl Zeiss). For certain experiments, P7 Purkinje cells from lobules III and IV/V and P21 Purkinje cells from lobules III-VIII were imaged.

For Figure 2A, z stack images of dendritic spines were acquired using an 63 × /1.4 Plan-Apochromat oil immersion objective (Carl Zeiss) at 2048 × 2048 pixels per frame, with a zoom factor of 3 and 0.4 μm z-steps. For each Purkinje cell, two z stack images of isolated distal dendrites were obtained, one from the deepest molecular layer depth bin and another from the most superficial bin. Each image included 1 or 2 distal dendrite segments.

#### **Antibodies**

We used the following primary antibodies: goat anti-GluD2 (Santa Cruz Biotechnology or Frontier Institute; 1:200), rabbit anti-HA (Cell Signaling Technology; 1:500), guinea pig anti-vGluT1 (Millipore Sigma or Frontier Institute, 1:200), guinea pig anti-vGluT2 (Millipore Sigma, or Frontier Institute, 1:200). In some MADM experiments, chicken anti-GFP (Aves; 1:500), rabbit anti-DsRed (Clontech; 1:500) were used.

#### Image analysis and processing

Imaris 9.3 FilamentTracer (Oxford Instruments) was used to trace the dendrites of cerebellar Purkinje cells from z stack confocal images (see above). Dendrites were traced using semi-automatic AutoPath and Manual modes with a fixed dendrite diameter of 5 pixels. The dendrite beginning point was defined as the location where the primary dendrite thickness is 8 µm in diameter for P14 and older Purkinje cells. For Purkinje cells at P7 and P10, because the primary dendrites tend to be thicker than that of older ages (see Figures 4C1 and 4C4), the thickness at the dendrite beginning point was defined as 10 μm in diameter. All dendritic protrusions longer than 2.5 µm were traced as dendrites. Only three dendritic segments were allowed to form a single dendrite branch point. After tracing all the dendrities, total dendritic length, total number of branch points and total number of dendritic segments were automatically computed by the software and obtained via the Statistics function. Images in Figure 4J were obtained by the Snapshot function of Imaris9.3. For all the other reconstructed dendritic tracing images shown in the figures, the traced dendrites ("filament" objects) were converted to a z stack image of a dendritic skeleton using the Create Channel function of Imaris9.3 XTension, and the z projection images were created by maximum intensity projection using ImageJ.

Quantification of dendrite branch points and dendrite length in the molecular layer depth bins were performed as follows. To determine the heights of molecular layer depth bins for each Purkinje cell, two points were marked in an orthogonal view to the x-y plane at the superficial surface of the molecular layer on each side of the Purkinje cell where no labeled dendrites existed (the molecular layer surface was visible by background fluorescent signal). A straight line connecting the two points was drawn and defined to be the superficial surface of the molecular layer. Another straight line passing through the dendrite beginning point was drawn parallel to the superficial surface of the molecular layer. When the Purkinje cell had multiple primary dendrites, the dendrite beginning point of the longest dendrite was used. The region between those two lines was defined as the molecular layer, and the distance between the lines was divided equally into five sublayers, which constitute the molecular layer depth bins. The branch points or dendrites above the 5<sup>th</sup> (most superficial) bin and those below the 1<sup>st</sup> (deepest) bin were included into the 5<sup>th</sup> and 1<sup>st</sup> bins, respectively. To quantify the dendrite branch points in each bin, x-y coordinates of all branching points were obtained via the FilamentTracer Statistics function. The x-y coordinates were rotated and translated so that the molecular layer was parallel to the x axis. The dendrite branch points in each bin were sorted according to their y coordinates. To quantify dendrite lengths, the traced dendrites were converted to three-dimensional dendritic skeletons using the Create Channel function of Imaris9.3 XTension. The dendritic skeleton had a uniform dendritic thickness (5 pixel). The images were opened using ImageJ (or Fiji, NIH), rectangular selections of each bin were made using the ROI Manager, and signal intensities of each ROI were measured from all of the z sections and summed. The resulting signal intensities were divided by the total signal intensities to determine the relative dendrite lengths in each bin. Normalized number of dendritic branch points or normalized dendrite length in each bin was calculated as a ratio to the total number of dendritic branch points or the total dendrite length across the dendritic tree, respectively.

Quantification of head widths of dendritic protrusions (Figure 2B) and spine densities (Figure 2C) were performed using ImageJ (NIH), blind to the genotypes and molecular layer depth bins. For each protrusion oriented into the x-y plane, the largest diameter of the protrusion head was drawn with a straight line perpendicular to the protrusion shaft and quantified as the head width. For quantification of spine density (Figure 2C), we first classified dendritic protrusions as spines and filopodia. We defined "spine" as a mushroom-shaped dendritic protrusion with a spine neck thinner than the spine head, while "filopodia" as a dendritic protrusion whose head is as thin as the stem. We randomly chose and measured the spine head width of 30 such typical "filopodia" and "mushroom spines" from the Purkinje cell images used for the quantification in Figure 2A. The distributions of head width of mushroom spine and filopodia were sufficiently bimodal (mushroom spine, mean head width = 0.385 μm, SD = 0.0594; filopodia, mean head width = 0.184 μm, SD = 0.050), justifying classification of these processes based on their head width. We used the cut-off of 0.2665 μm ( = mean - 2SD of mushroom spine head width) to classify dendritic processes as "spine" (head width  $\geq 0.2665 \mu m$ ). We then randomly selected one or two dendritic segments from each of the z stacked confocal images, quantified the number of all dendritic





protrusions oriented into the x-y plane across all the z sections, their head widtsh, and the lengths of the dendritic segment. The dendritic spine density was calculated by dividing the number of spines (head width ≥ 0.2665 µm) by the length of dendritic segment.

For quantification of GluD2 levels in Figure S6C, GluD2 levels in cytosolic regions of the somata of labeled and neighboring nontransfected control Purkinje cells were quantified. Background GluD2 levels were defined as the GluD2 levels in the internal granular layer and were subtracted from the somata measurements. The percentages of resulting GluD2 intensities in the labeled cells to those of non-transfected control Purkinje cell were defined to be the relative GluD2 levels. To quantify normalized vGluT1 or GluD2 levels in dendrites at P7 (Figures 2 and 5), dendritic regions of a labeled cell were selected using Otsu's thresholding of GFP or tdT (Figure 2), or GluD2 (Figure 5) and the mean intensities of vGluT1 or GluD2 were measured. The mean intensities of neighboring vGluT1-positive molecular layer regions (for Figure 2) or non-transfected dendrites (for Figure 5) were also measured. Background intensities were defined as the darkest regions in the external granule layer and subtracted from the selected regions. The resulting values of sKO dendrites were divided by those of non-transfected dendrites and normalized to average vGluT1 or GluD2 values determined in the same manner from the dendrites of control cells. To quantify normalized GluD2 levels in dendrites at P21 (Figure 5; Figure S5), tdT<sup>+</sup> dendrite regions were selected using Otsu's thresholding and GluD2 levels in the tdT<sup>+</sup> regions were recorded. Control GluD2 levels were defined as neighboring unlabeled molecular layer regions selected using the Rectangular tool. Background intensities were defined as the signal in neighboring interneurons' nuclei and subtracted from the selected regions. The percentage of GluD2 levels of labeled dendrites to that of non-transfected regions was normalized to that of control Purkinje cell dendrites expressing only tdT.

GluD2 overexpressing Purkinje cells in Figure S5 often had other labeled cells in their vicinity, due to their increased dendrite thickness. Therefore, to highlight their morphologies, masked images were created for Figures S5C, S5D2, and S5E. To do so, dendrites belonging to other cells were removed from each z section using ImageJ (NIH). The modified images were then opened in Imaris9.3 and Surface objects were created based on the modified images. The original raw images were then masked using the Surface objects.

#### **Evaluating baseline parameters for controls**

In this study, we used different methods to disrupt GluD2: IUE (GFP and Cre) into control (Ai14) or GluD2<sup>fl/fl</sup> embryos (sKO), MADM, IUE (GFP or tdT) into WT or GluD2<sup>-/-</sup> embryos (gKO), and CRISPR-Cas9-based IUE into wild-type or Cbln1<sup>-/-</sup> embryos (gKO). While each experiment has a control, each control was on a different genetic background and may thus have shown different baseline parameters for Purkinje cell dendrites. For example, in Figure 1, the Ai14 controls (for IUE) have more branch points and a longer total dendritic length than MADM control cells (GluD2+/- cells in the same sample). We statistically compared all four control conditions used in this study (Ai14 controls, MADM controls, WT controls for gKO, and sg-LacZ/WT controls for csKO) and found that only Ai14 controls have a significantly greater number of total branch points and total dendrite length than gKO controls or csKO controls (oneway ANOVA followed by Tukey's multiple comparison test; total branch points, \*p < 0.05 for Ai14 control versus csKO control; total dendrite length, \*p < 0.05 for Ai14 control versus gKO control, and \*\*p < 0.01 for Ai14 control versus csKO control; p values were calculated by Tukey's multiple comparison of all 4 groups; n = 5, 6, 7, 5 cells from two mice each for Ai14, MADM, gKO and csKO controls, respectively). There were no significant differences between any other pairs among MADM, gKO and csKO controls. These results indicate that the Purkinje cells of our Ai14 mice expressing GFP and Cre have a larger dendritic tree. Such discrepancies in control base values may be due to differences in mouse genetic background and underscore the importance of control samples of similar conditions (including mouse strain and plasmids introduced by IUE). Likewise, our observations were controlled for in each of our experiments (MADM allows comparison to within-sample control cells).

### **QUANTIFICATION AND STATISTICAL ANALYSIS**

Prism 8.4 (GraphPad) and Excel (Microsoft) were used for data analysis and plotting. All statistical tests were performed using Prism 8.4 (GraphPad).

# **MODELING AND SIMULATION METHODS**

## **Overview of Basic Algorithm**

We simulated Purkinje cell (PC) dendritic tree growth on a single 2D plane pierced by orthogonal intersecting parallel fibers. Specifically, we started with 3 adjacent PCs at an early developmental stage (Figure 8A). Growth occurs either through extension of dendritic segments from their terminals (elongation) or interstitial branching from an existing non-terminal segment (which we hereafter refer to as branching). Both elongation and branching result in the growth of a new segment. Every dendritic segment consists of a straight line that starts and ends at nearby discretized lattice points on the 2D parallel fiber (PF) grid. Each such lattice point corresponds to a potential PF  $\rightarrow$  PC synapse, which is then realized when a dendritic segment occupies that lattice point. Note that in our simplified 2D planar growth model, we do not consider influences from PC's at other 2D planes. We model only PF→PC synapses and omit the impact of climbing fiber inputs.

The dendritic segments of a modeled PC can be oriented along one of 16 directions, corresponding to 16 possible nearby lattice displacements between the start and end of every dendritic segment:  $(\Delta x, \Delta y) \in \{(0, \pm 1), (\pm 1, 0), (\pm 1, \pm 1), (\pm 1, \pm 2), (\pm 2, \pm 1)\}$ (Figure 8C4). These 16 choices of lattice displacements correspond to an approximate angular separation of 22.5 degrees between adjacent directions. Our final lattice grid of PFs extends across 3×38 = 114 lattice points horizontally and 38 lattice points vertically.





We model 3 adjacent PC's under 4 different conditions: (1) WT, (2) GluD2 sparse knockout (sKO) (i.e., modifying growth parameters of the central PC only), (3) global knockout (gKO) (changing the growth parameters of all three PCs), or (4) GluD2 sparse overexpression (OE). The probability of successful elongation or branching at any given point to one of the 16 directions follows the general rules below for all PCs, albeit with different growth parameters for WT and GluD2 knockout cells:

- 1. To restrict excessive dendrite turning, elongation from a terminal point is limited to 3 directions (0 degrees or approximately ± 22.5 degrees) relative to the orientation of the terminal segment from which elongation is initiated.
- 2. Branching can occur in any one of the 16 directions.
- 3. The probability of elongation and branching upward is higher (mimicking a presumptive attractant from the pial surface).
- 4. To enforce lack of collisions, neither elongation nor branching can result in the creation of a new dendritic segment that terminates at a lattice point already occupied by a previously grown dendritic segment, and no new segment can intersect any such previous segment.
- 5. In addition, both the probabilities of elongation and branching to regions with a high density of nearby dendritic segments are diminished through specific modeling of longer range dendro-dendritic repulsion from the same tree, as well as competition from the dendritic tree of neighboring cells.

To execute these rules, at each iteration we randomly picked an occupied lattice point of one of the three existing dendritic trees. Any such chosen lattice point can belong to one of three classes: (1) it is a terminal point on the tree, in which case, in our model, elongation is the only possibility for growth from this point; (2) it is a non-terminal point from which the dendrite extends in two directions, in which case branching is the only possibility for growth from this point; (3) it is a branch point in which the tree already extends in three directions, in which case we do not allow further growth from this point. For the randomly chosen point, our model makes a probabilistic decision as to whether or not to elongate or branch when feasible.

More specifically, let E and B be the events that successful elongation or branching, respectively, actually occurs from a candidate growth point on the tree. The probability P(E) (or P(B)) of successful elongation (or branching) from that growth point is not necessarily 1 and could actually fail due to hard constraints involving collision avoidance or soft factors due to longer range repulsion in all possible directions. However, when a successful elongation or branching event actually occurs, the direction  $\theta$  along which growth occurs is also chosen probabilistically from the conditional distributions  $P(\theta|E)$  for elongation and  $P(\theta|B)$  for branching. In general, directions  $\theta$  in which appreciable dendrodendritic repulsion is far away or directions that are closer to the upward direction are favored in the distributions  $P(\theta|B)$  and  $P(\theta|B)$ . This process of randomly choosing a growth point, randomly deciding whether or not to grow, and then randomly deciding which direction to grow, is repeated for 2000-4000 iterations to grow all three trees.

Below, we describe in sequence how we modeled dendrodentritic repulsion, how this repulsion determines the conditional probability distributions  $P(\theta|E)$  and  $P(\theta|B)$  for which direction  $\theta$  to elongate or branch respectively, and how the total level of repulsion, along with intrinsic drives for growth, determine the probabilities P(E) and P(B) of successful growth or elongation in the first place. We then describe which growth parameters are different in WT and GluD2 knockout cells. Finally, we end with a high-level intuitive description of the key principles enabling our model to account for the experimental data.

#### Modeling dendrodentritic repulsion

We define  $r_i(x, y)$  to be the repulsion field of neuron i = 1, 2, 3, which always equals the convolution of the current dendritic tree with a spatially decaying kernel. The kernel occupies 17×17 lattice points with a central value of 1.875 and all other elements of the kernel fall of as (1/16). Euclidean distance from the center. This kernel, when convolved with the dendritic tree of neuron i, yields a spatially decaying repulsion field  $r_i(x, y)$  around each tree. Examples of the three repulsion fields are shown at an early growth state in Figure 8B. The growth of a given tree involves a total repulsion field r(x,y) that combines its own self-repulsion field with that of its neighbors. For example, for the middle cell,  $r(x,y) = 5 * r_1(x,y) + r_2(x,y) + 5 * r_3(x,y)$ ; this ensures that neighbor repulsion is five times stronger than self-repulsion.

# Repulsion as a function of angle determines which direction to grow

To determine the conditional probabilities  $P(\theta|E)$  and  $P(\theta|B)$  conditioned on a successful elongation (E) or branching (B) event, we first define a growth score  $s(\theta)$  that describes how favorable it would be to grow in a direction  $\theta$ , where  $\theta$  is one of the 16 possible directions for growth shown in Figure 7C4. For growth directions  $\theta$  in which a collision would occur,  $s(\theta) = 0$ , which effectively forbids growth. Otherwise,  $s(\theta) = \frac{d(\theta)}{r(\theta)} + b(\theta, y)$ . In the first term,  $d(\theta)$  is the distance along the growth direction  $\theta$  to the nearest lattice point (x,y) with nonzero repulsion r(x,y) and  $r(\theta)$  is the value of this repulsion. Thus directions  $\theta$  in which appreciable repulsion is far away yield a larger value of the ratio  $\frac{d(\theta)}{r(\theta)}$ , thereby increasing the growth score  $s(\theta)$ .

The second term  $b(\theta, y)$  promotes vertical growth, with increasing strength the closer the growth point is in y to the pial surface and the closer the growth angle  $\theta$  is to the upward direction. More specifically, we define  $f_y = \frac{y}{h_{MI}}$  to be the fraction of the vertical distance ythe growth point is to the height of the molecular layer  $h_{ML}$ . For angles  $\theta$  in which  $\Delta y \leq 0$ ,  $b(\theta, y) = \max(0.75, 1 - f_y)$ . For angles  $\theta$  in which  $(\Delta x, \Delta y) = (\pm 2, 1)$ ,  $b(\theta, y) = 0.5 \cdot f_y$ . For angles  $\theta$  in which  $(\Delta x, \Delta y) = (\pm 1, 1)$ ,  $b(\theta, y) = f_y$ . For angles  $\theta$  in which  $(\Delta x, \Delta y) = (\pm 1, 2)$ ,  $b(\theta, y) = 1.5 \cdot f_v$ . For the vertical  $\theta = 90$  degrees in which  $(\Delta x, \Delta y) = (0, 1)$ ,  $b(\theta, y) = 2 \cdot f_v$ . Basically, the vertical bias score simply increases linearly with both the height of the growth point and with the rank ordering of the possible slopes. Thus, in summary, the growth score  $s(\theta)$  is larger when appreciable repulsion is further away in direction  $\theta$ , and also larger when this direction is closer to





upward. However, it is 0 if growth in direction  $\theta$  would lead to a collision. Finally, this growth score determines the angular conditional probability distributions of growth through

$$P\bigg(\theta|E) = \frac{s(\theta)}{\sum_{\theta_{P}} s(\theta_{E})}, \quad P(\theta|B\bigg) = \frac{s(\theta)}{\sum_{\theta_{P}} s(\theta_{B})} \ .$$

Here, for elongation, the sum over  $\theta_E$  extends over only 3 angles: 0 degrees or approximately  $\pm$  22.5 degrees, relative to the orientation of the terminal segment from which elongation is initiated and  $P(\theta|E)$  can be nonzero only for these 3 angles, yielding a normalized probability distribution. Conversely, the sum over  $\theta_B$  extends over all 16 possible directions. In summary, these probabilities determine the randomly chosen angle of growth, by forbidding collisions, avoiding the repulsion field, favoring upward growth, and restricting dendritic turning for elongation but not branching.

#### A balance between total repulsion and intrinsic drive determines the decision to grow

We next describe how our model computes the probabilities P(E) and P(B) of successful elongation or branching events in the first place. Both these probabilities are inversely related to the total repulsion R<sub>TOT</sub> summed across all directions and directly related to overall growth drives  $E(n_{syn})$  and  $B(n_{syn})$ . These latter drives depend on the number of synapses  $n_{syn}$  already formed and stabilized by the tree and are decreasing functions of  $n_{\text{syn}}$ , reflecting that the total growth drive decays as the number of synapses increases. Thus, in our model, synapse formation acts as a soft slow-down inhibitor of dendritic growth. Specifically, the probabilities of successful growth are obtained by balancing the growth drives against the total repulsion through

$$P(E) = \min\left(\frac{E\left(n_{\text{syn}}\right)}{\sqrt{R_{TOT}}}, 1\right), \ P(B) = \min\left(\frac{B\left(n_{\text{syn}}\right)}{R_{TOT}^{0.8}}, 1\right).$$

Thus, high total repulsion  $R_{TOT}$  in the local vicinity of a candidate growth point and larger numbers of stable synapses  $n_{syn}$  across the entire tree both decrease the probabilities of successful elongation or branching from that growth point. We next describe how we compute the total repulsion  $R_{\mathrm{TOT}}$  and the growth drives  $E(n_{\mathrm{syn}})$  and  $B(n_{\mathrm{syn}})$ .

The total repulsion  $R_{\mathsf{TOT}}$  is defined as follows. Let  $R(\theta)$  be a measure of the repulsion in direction  $\theta$ . We define  $R(\theta) = \min\left(\frac{1}{s(\theta) - b(\theta, y)}, 200\right)$  where  $s(\theta)$  is the growth score defined above. Basically, in a direction  $\theta$  in which growth would lead to a collision,  $R(\theta)$  would take a maximal penalizing value of 200. Conversely, in a direction  $\theta$  in which growth would lead to no such collision,  $R(\theta) = \frac{r(\theta)}{d(\theta)}$ , where, again,  $d(\theta)$  is the distance along the growth direction  $\theta$  to the nearest lattice point (x,y) with nonzero repulsion r(x,y), and  $r(\theta)$  is the value of this repulsion. Then we have  $R_{TOT} = \sum_{\theta} max(1,R_{\theta})$ . In simulations,  $R_{TOT}$  is typically on the order of  $10^0$  to  $10^1$ .

Now the growth drives are given by

$$E(n_{\text{syn}}) = 0.2 + \frac{\lambda_E}{e^{\frac{n_{\text{syn}} - \theta_E}{N_E^*}} + 1}, \quad B(n_{\text{syn}}) = 0.05 + \frac{\lambda_B}{e^{\frac{n_{\text{syn}} - \theta_B}{N_B^*}} + 1}.$$

Both are sigmoidal decreasing functions of the number of synapses  $n_{\text{syn}}$  already formed.  $\theta_{E}$  and  $\theta_{B}$  are threshold parameters; when  $n_{\text{syn}}$  is significantly above either threshold, the corresponding growth drives starts to diminish. Correspondingly,  $N_E^*$  and  $N_B^*$  set the scale, in terms of number of synapses above threshold, at which diminished growth starts to set in. Finally,  $\lambda_E$  and  $\lambda_B$  are overall constants that contribute to the corresponding growth drive when  $n_{\text{syn}}$  is at the corresponding threshold  $\theta_E$  or  $\theta_B$ .

For wild-type PCs,  $N_E^* = 1000$ ,  $\theta_E = 500$ , and  $\lambda_E = 0.5$ . This yields a modulation of  $E(0) \approx 0.5$  at the beginning of growth and an  $E(1000) \approx 0.4$  at a late stage of growth. Also, for wild-type PCs,  $N_B^* = 500$ ,  $\theta_B = 250$ , and  $\lambda_B = 10$  for wild-type PCs. This yields a modulation of  $B(0) \approx 6.3$  at the beginning of growth and a  $B(1000) \approx 1.9$  at a late stage of growth. Then when combined with the total repulsion, for wild-type PCs the elongation probability P(E) is in the range 0.01 to 0.02 in early growth and is close to 0.009 in later growth stages. In contrast, the branching probability P(B) is typically in the range 0.01 to 0.025 in early growth stages, and close to 0.007 in later stages.

#### Parallel Fiber Expansion

Once the dendritic trees for each condition have elaborated enough such that branches stop growing (due to excessive repulsion in every direction), we expand the grid of parallel fibers available as synaptic partners. We do so by adding a set of rows and 3 times that number of columns (due to having 3 cells). After the expansion, each cell has an equal amount of excess space to grow both upward and to either side. The parallel fiber lattice starts as a 90  $\times$  30 lattice, and then expands to 102  $\times$  34 and finally to 114  $\times$  38.

#### Modeling the loss and overexpression of the GluD2 receptor

To simulate the effect of losing the GluD2 receptor, we make two changes:

1. We change  $\lambda_E$  and  $\lambda_B$  from  $(\lambda_E, \lambda_B)_{WT} = (0.5, 10)$  to  $(\lambda_E, \lambda_B)_{KO} = (4, 0.5)$ . Thus, the intrinsic growth drive for elongation is increased, while the growth drive for branching is decreased. We justify this change based on experimental evidence that there are fewer branching points in the 2D plane for knockout cells than for WT cells. Also, a decrease in branching likelihood





simulates a tree being less effective at growing outward (which involves growing at more angles than just upward or at a 22.5degree offset from upward). Because this model is probabilistic and each branch is final, having a decrease in likelihood of branching simulates the process of two growth cones, one from a knockout cell and one from a wild-type cell, competing for a synapse with a PF and the knockout growth cone losing and thus retracting. Then the likelihood of elongation is also increased so as to compensate for the consequent reduction in number of synapses formed—the PC dendrites extend throughout the molecular layer even without the GluD2 receptor; indeed, GluD2 sKO cells overextended dendrites beyond the upper border of the molecular layer at P10 (Figure S4J).

2. The knockout cell is less effective at forming synapses because the deletion of GluD2 will diminish its ability to stabilize synapses. Experimental evidence also suggests that only 60% of synapses are retained in a GluD2 knockout condition. Thus, we stochastically count 60% of the number of synapses total in a given knockout cell (used to parametrize the  $E(n_{syn})$  and  $B(n_{syn})$ curves), which is on average equivalent to replacing  $n_{\text{syn}}$  with  $0.6 \cdot n_{\text{syn}}$  for the knockout cell. This means that the knockout cell will experience a diminished reduction in growth drives  $E(n_{syn})$  and  $B(n_{syn})$ .

Overall, this simple change of only two parameters  $\lambda_E$  and  $\lambda_B$  in going from WT to knockout is sufficient to account for two striking experimentally observed morphological phenotypes: square dendritic trees in the WT condition (where all three cells are WT), and an inverted triangular dendritic tree for the middle knockout cell in the sKO condition (with a WT neighbor on either side). While we made various choices about model parameters, we do not claim that these are the only sets of parameters that will result in these phenotypes. This is certainly one such set that mimics the experimental data, but there is likely a diversity of parameter choices that can explain the data.

To simulate the effect of overexpressing the GluD2 receptor, we simply change  $\lambda_E$  and  $\lambda_B$  from  $(\lambda_E, \lambda_B)_{WT} = (0.5, 10)$  to  $(\lambda_E, \lambda_B)_{OF} = (0.5, 10)$  to  $(\lambda_E, \lambda_B)_{OF} = (0.5, 10)$  to  $(\lambda_E, \lambda_B)_{OF} = (0.5, 10)$ (0.005,50). Thus, the effect is the opposite of what happens in the KO case. Note that many branches that would grow three-dimensionally are lost by our 2D model.

#### Key principles underlying model behavior

Regardless of detailed parameter choices, a few key principles explain the behavior of the model. First, in going from WT to knockout, elongation becomes favored while branching is suppressed. In the sKO condition, the suppressed branching forces the knockout cell to lose the competition with its WT neighbors to grow its tree by forming synapses in the deep layers where two WT and one sKO tree are all initially present. Thus, the WT neighbor dendritic trees invade the territory of the sKO tree and prevents its outward branching in the deep layers. However, the enhanced elongation of the sKO cell relative to WT cells enables it to reach the superficial layers before the WT does. Moreover, even if the WT tree catches up to the sKO tree in the superficial layers, it has a more diminished drive for branching (reduced  $E(n_{syn})$  and therefore reduced P(B)) because it has already formed more synapses than the sKO tree due to its already winning the competition in the deep layers (i.e., it has a larger  $n_{syn}$ ).

Thus, a combination of three effects enables the sKO cell to win the competition for territory with its WT neighbors in the superficial layers despite the fact that it lost the competition in the deep layers: (1) the sKO tree reaches the superficial layer earlier, (2) the WT cell has diminished drive for branching in the superficial layers due to a larger number of already formed synapses in the deep layers, and (3) the sKO has a less diminished drive for branching in the superficial layers due to formation of fewer synapses in the deep layers. Combined, these effects explain the emergence of the inverted triangular phenotype of the sKO cell through the loss of a competition with its WT neighbors in the deep (superficial) layers.